Irregularities observed at the edge of a mid-latitude ionospheric trough following a geomagnetic storm

Joseph F Helmboldt[1]

[1]Naval Research Laboratory

February 9, 2023

Abstract

This manuscript presents the analysis of data from multiple ground- and space-based sensors in the North American region before, during, and after the 12 Oct. 2021 geomagnetic storm. The data show the formation and equatorward propagation of a density trough, which manifested within bottom-side and top-side electron density data as well as within maps of total electron content (TEC). During the recovery phase on the 13th, the equatorward edge of the trough settled at around 30° latitude and exhibited a steep density gradient. By the 14th, this sharp boundary had disappeared. Near this edge on the 13th, small-scale irregularities formed. The impact of these was observed within Global Positioning System (GPS) data as elevated rate of TEC index (ROTI) and presented as strong 35 MHz scintillations of cosmic radio sources as well as spread-F within ionograms from multiple digisonde systems. GPS and 35-MHz data demonstrated that the irregularity region was narrowly confined ([?]5deg wide) near the trough edge. The 35-MHz scintillation data also showed that the irregularities were moving relatively slowly at ˜7 m s-1, likely toward the southeast. Density and velocity measurements demonstrate that the conditions near the trough boundary we highly favorable for the gradient drift instability (GDI) with the one-dimensional growth rate estimated to be ˜0.01 s-1. Since these conditions persisted for many hours, this growth rate was more than sufficient for the GDI to be considered the primary driver of irregularity formation in this case.

Irregularities observed at the edge of a mid-latitude ionospheric trough following a geomagnetic storm

J. F. Helmboldt[1]

[1]US Naval Research Laboratory, 4555 Overlook Ave. SW, Washington, DC 20375, USA.

Key Points:

- A multitude of ground- and space-based sensors were used to study a storm-induced trough, its evolution, and its impact over North America.
- Irregularities at the equatorward edge of the trough impacted radio frequency systems from a few MHz to 1.5 GHz.
- Space-based in situ and remote sensing data point to the gradient drift instability as the most likely driver of irregularity formation.

Corresponding author: J. F. Helmboldt, `joseph.helmboldt@nrl.navy.mil`

Abstract

This manuscript presents the analysis of data from multiple ground- and space-based sensors in the North American region before, during, and after the 12 Oct. 2021 geomagnetic storm. The data show the formation and equatorward propagation of a density trough, which manifested within bottom-side and top-side electron density data as well as within maps of total electron content (TEC). During the recovery phase on the 13$^{\text{th}}$, the equatorward edge of the trough settled at around 30° latitude and exhibited a steep density gradient. By the 14$^{\text{th}}$, this sharp boundary had disappeared. Near this edge on the 13$^{\text{th}}$, small-scale irregularities formed. The impact of these was observed within Global Positioning System (GPS) data as elevated rate of TEC index (ROTI) and presented as strong 35 MHz scintillations of cosmic radio sources as well as spread-F within ionograms from multiple digisonde systems. GPS and 35-MHz data demonstrated that the irregularity region was narrowly confined ($\lesssim$5° wide) near the trough edge. The 35-MHz scintillation data also showed that the irregularities were moving relatively slowly at $\sim$7 m s^{-1}, likely toward the southeast. Density and velocity measurements demonstrate that the conditions near the trough boundary we highly favorable for the gradient drift instability (GDI) with the one-dimensional growth rate estimated to be $\sim$0.01 s^{-1}. Since these conditions persisted for many hours, this growth rate was more than sufficient for the GDI to be considered the primary driver of irregularity formation in this case.

Plain Language Summary

Earth's ionosphere, the ionized portion of the upper atmosphere, is a dynamic environment, often beset with irregularities and disturbances that interfere with radio frequency signals that travel through it. In this regard, mid-latitudes are usually quite tame relative to the equatorial and polar regions. However, when significant geomagnetic disturbances, or "storms," occur, this normally placid region can become anything but. This paper presents the results of a study that examines the impact of a storm over North America, using several space- and ground-based sensors. Of particular interest is the formation of a density trough that moves toward the equator after the onset of the storm. Multiple sensors show evidence of this trough and still others show a preponderance of small-scale irregularities (on the order of 100 meters to a few kilometers) near its southern boundary. A holistic analysis indicates that these irregularities are consistent with a turbulent cascade moving relatively slowly, likely toward the south or southeast. Conditions near the trough were observed to be conducive with the so-called gradient drift instability. This is known to be a primary driver of irregularity formation within other settings, and appears to be the culprit in this case as well.

1 Introduction

At mid-latitudes, Earth's ionosphere is generally a quiet and uneventful environment when compared to the more active and dynamic settings of the equatorial and arctic/auroral regions. There are, of course, exceptions to this general statement, especially under geomagnetic storm conditions. These events erode the plasmasphere and initiate plume formation, leading to storm enhanced densities (SEDs) at mid-latitudes with telltale morphologies (Foster et al., 2002). This is related to a strong sub-auroral polarization stream (SAPS), which also leads to the formation of a density trough. This trough results from an increase in the recombination rate in the F-region due to an enhancement in ion-neutral heating related to the strong SAPS electric field (Schunk et al., 1976).

Generally, during geomagnetically active periods, such density troughs have been observed to move equatorward and to have a relatively sharp boundary on the equatorial edge (Krankowski et al., 2009; Shinbori et al., 2018). The combination of these two factors implies that near this edge, the conditions could be ripe for the formation of irregularities that are unusually strong for mid-latitudes via, e.g., the gradient drift instability (GDI; Linson and Workman (1970)). Indeed, isolated incidences of intense microwave-frequency scintillations have been observed with specialized Global Positioning System (GPS) ground-based sensors at mid-latitudes near an equatorward-propagating trough following geomagnetic activity (Ledvina et al., 2002; Rodrigues et al., 2021).

This manuscript adds to this growing body of work with similar analysis of data collected around the geomagnetic storm that occurred on 12 Oct. 2021. In this case, a unique new instrument, the Deployable Low-band Ionosphere and Transient Experiment (DLITE; Helmboldt et al. (2021)), was used to measure scintillations at a much lower frequency, 35 MHz, from New Mexico and Maryland. These measurements combined with GPS and digisonde data as well as spacecraft observations support the conclusion that a turbulent cascade was triggered by the GDI at the edge of the trough associated with this storm. This resulted in relatively intense irregularity activity impacting radio frequency systems from frequencies of a few MHz to 1.5 GHz. The data and analysis are described below in Sec. 2 with conclusions discussed in more detail in Sec. 3.

2 Data and Analysis

2.1 The Storm and Mid-latitude Features

The storm that occurred on 12 Oct. 2021 was initiated by a coronal mass ejection, which impacted just before 02 UT. The impact actually initiated a double storm with minima in the Dst index at around 06 and 14 UT. These are evident in the upper panel of Fig. 1, which shows the Dst time series from 11 Oct. (day of the year, DOY= 284) through the end of 14 Oct. To illustrate the impact on mid-latitude electron density, vertical total electron content (TEC) maps were obtained at five-minute cadence from the Madrigal database. A keogram at a fixed longitude of $-100°$ is shown in Fig. 1 with the colormap set to highlight the nighttime ionosphere when the trough is more prevalent/obvious. As the Dst index plummets, a narrow trough appears and moves continuously equatorward during the night of 12 Oct. (DOY= 285). When the lower boundary moves below $\sim 40°$ latitude, the trough broadens significantly. During the recovery phase on the night of 13 Oct. (DOY= 286), the lower trough boundary has settled at $\sim 30°$ latitude and is quite sharp. By the night of 14 Oct., this clear edge has eroded substantially. Within the keogram, times of 03 and 06 UT are highlighted with green dashed lines and will be explored in more detail below.

To search for evidence of GPS scintillations/irregularities, publicly available data from over 2,000 GPS receivers in the continental United States (CONUS) were obtain in receiver independent exchange (RINEX) format and processed to look for rapid variations in TEC. These data were predominantly recorded at a cadence of 30 s. Consequently, they were used to compute the rate of TEC index (ROTI) by computing the difference in TEC between samples separated by 30 s for each satellite/receiver pair. Using pierce point locations at an altitude of 300 km and an elevation limit of $>30°$ to avoid multi-path effects, the measurements of ROTI^2 were averaged within $0.5° \times 0.5° \times 1$ min. bins in latitude/longitude/UT. To make a keogram similar to the one created for vertical TEC, these were further averaged to a cadence of 5 min. and between longitudes of $-105°$ and $-95°$. The square root of the result is shown as a ROTI keogram in Fig. 1. From this, one can see elevated ROTI at the boundary of the trough during the nights of 12 and 13 Oct.

To demonstrate the impact of the trough and its equatorward movement between 12 and 13 Oct. on electron density and not just TEC, we also show time series of the `foF2` parameter obtained from nine digisonde systems from throughout North America in the bottom panel of Fig. 1, color-coded by latitude. One can see that the lowest latitudes are not affected by the trough as they are too far south. The highest latitudes (up to $\sim 45°$), however, show noticeably lower densities, especially during the night of 13 Oct.

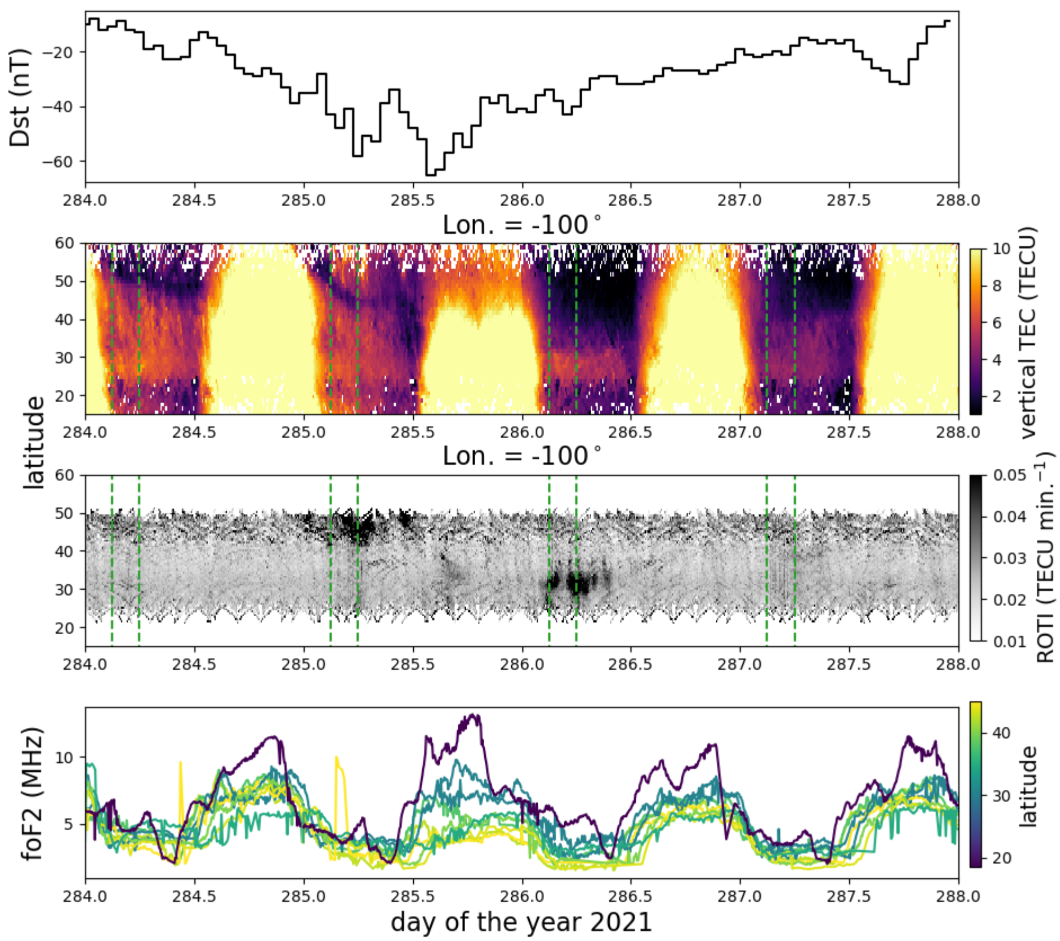

Figure 1. Plots showing the 12 Oct. 2021 storm and its ionospheric impacts. Upper: Dst index time series from 11-14 Oct. Middle: Keograms for vertical TEC and ROTI at a longitude of $-100°$; times of 03 and 06 UT that will be highlighted in subsequent figures are indicated with vertical dashed green lines. Bottom: Time series of `foF2` from nine North American digisonde systems, color coded by latitude.

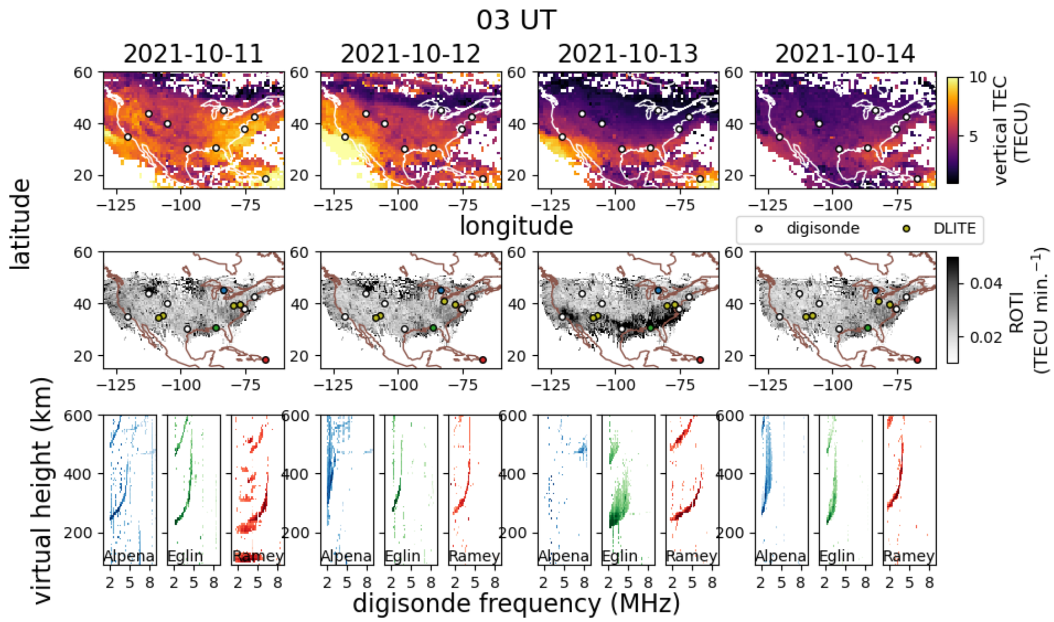

Figure 2. Upper row: For 11–14 Oct. 2021, maps of vertical TEC at 03 UT with locations of digisonde systems indicated with white points. Middle row: Maps of ROTI (one-hour bin) with digisonde locations and DLITE pierce points toward Cyg A and Cas A highlighted. Bottom row: Ionograms (O-mode only) from three example digisondes. The colormaps used correspond to the colors of the circles used to indicate the digisondes' locations in the middle row of panels.

At this time, multiple digisondes had `foF2` at the minimum frequency used (∼2 MHz), implying the ionosphere all but disappeared to those radars.

Fig. 2–3 show maps of vertical TEC and ROTI at example times of 03 and 06 UT on each date between 11 and 14 Oct. 2021. In this case, the measurements of ROTI^2 were left at a resolution of 0.5° × 0.5° in latitude/longitude but were averaged within ±30 minutes of the central time (i.e., 03 or 06 UT). The maps show the square root of the results. Within each panel, the locations of the North American digisonde systems with available data are shown with white points.

On the ROTI maps, three example digisondes are highlighted in color: Alpena, Michigan (blue); Eglin Air Force Base, Florida (green); and Ramey Air Force Base, Puerto Rico (red). Ionograms (O-mode only) from these three systems are shown below the ROTI maps for each date/time. With the exception of some interference issues, the Ramey ionograms show reasonably well defined, typical-looking traces. The Alpena ionogram shows some evidence of broadening at both 03 and 06 UT on 12 Oct. when the enhanced ROTI region was nearby and essentially disappears on the 13$^{\text{th}}$, recovering somewhat on the 14$^{\text{th}}$. The Eglin ionograms appear relatively normal except on the 13$^{\text{th}}$ when there is a substantial amount of spread-F at both 03 and 06 UT and a significant decrease in density at 06 UT. These incidences of spread-F occurred when the lower trough boundary moved over the region. Similar behavior was observed within the data for the digisonde in Austin, Texas, which was also at the trough edge on 13 Oct.

Within the ROTI maps in Fig. 2–3, yellow points indicate 300 km altitude pierce points associated with the DLITE systems operating in New Mexico (at 34.07°N, 107.63°W) and Maryland (at 38.56°N, 77.06°W). Each DLITE system is an array of four inverted vee dipole antennas designed for the Long Wavelength Array (Hicks et al., 2012). These

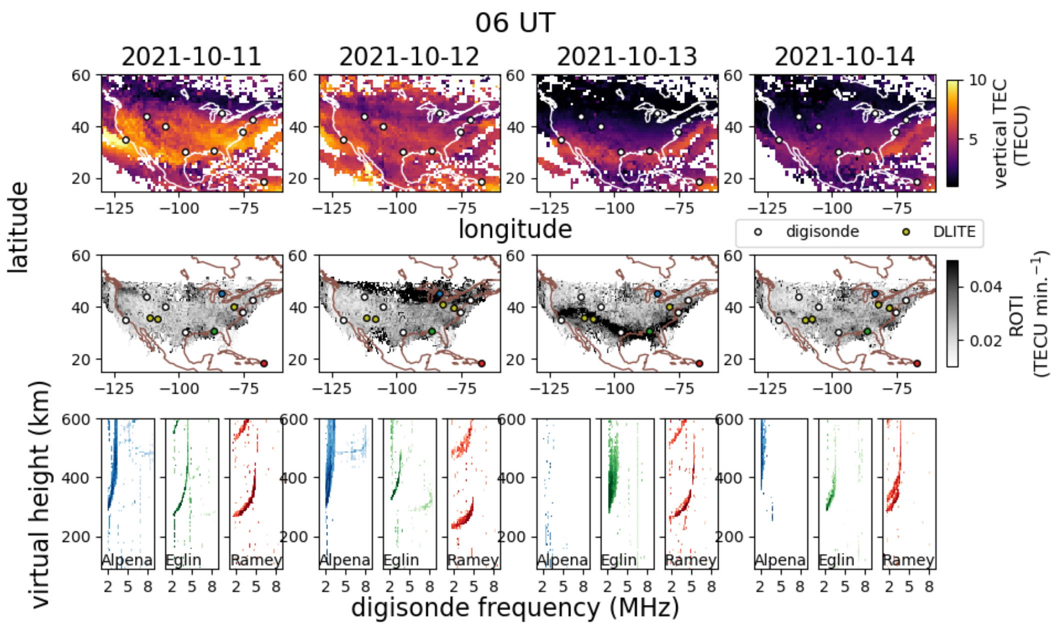

Figure 3. The same as Fig. 2, but for 06 UT.

antennas are separated from one another by ∼200–450 m and used together as an interferometric telescope. They observe the entire sky in a 30–40 MHz band, using time and frequency difference of arrival (TDOA and FDOA, respectively) methods to resolve individual cosmic radio sources from one another. There are six such sources that are bright enough to be observed with a DLITE system from the Northern Hemisphere, 2–4 of which are visible at the same time. The brightest two of these by far are Cygnus A (Cyg A) and Cassiopeia A (Cas A), which are observable together for several hours per day are are consistently the best objects to use for scintillation studies at 35 MHz. The pierce points shown in Fig. 2–3 are for these two sources.

As detailed by Helmboldt et al. (2021), the level of 35 MHz scintillations can be measured with each pair of antennas, or "baseline," by using ∼1 hour of data to make a TDOA, FDOA image of the sky. With this amount of data, sources are well resolved from one another and easily identifiable given the known antenna locations. Scintillations cause a plateau-like artifact to form in the FDOA direction only, associated with the scintillating source. The magnitude of this plateau relative to the peak observed intensity provides a means to measure the S_4 index. Such measurements can also be converted to the C_kL irregularity index, which is independent of frequency and observing geometry and is proportional to the integrated electron density variance within the irregularity region. The methods used to do this are described in detail by Helmboldt et al. (2021) and show good agreement with similar irregularity measurements made with a nearby dynasonde radar system (Helmboldt & Zabotin, 2022).

Fig. 4 shows images of the peak intensity as a function of time and either TDOA or FDOA for the longest baseline of the New Mexico system, DLITE-NM, and the system near Pomonkey, Maryland, DLITE-POM, which are from TDOA, FDOA images generated at a ∼20 min. cadence. For DLITE-NM, this is a ∼420-m east/west baseline, and for DLITE-POM, the baseline is ∼350-m north/south. One can see that prior to 13 Oct. (DOY= 286), the DLITE-POM data were quite noisy, which was due to interference from a faulty utility pole at the site (bad insulators). The array was shut down temporarily

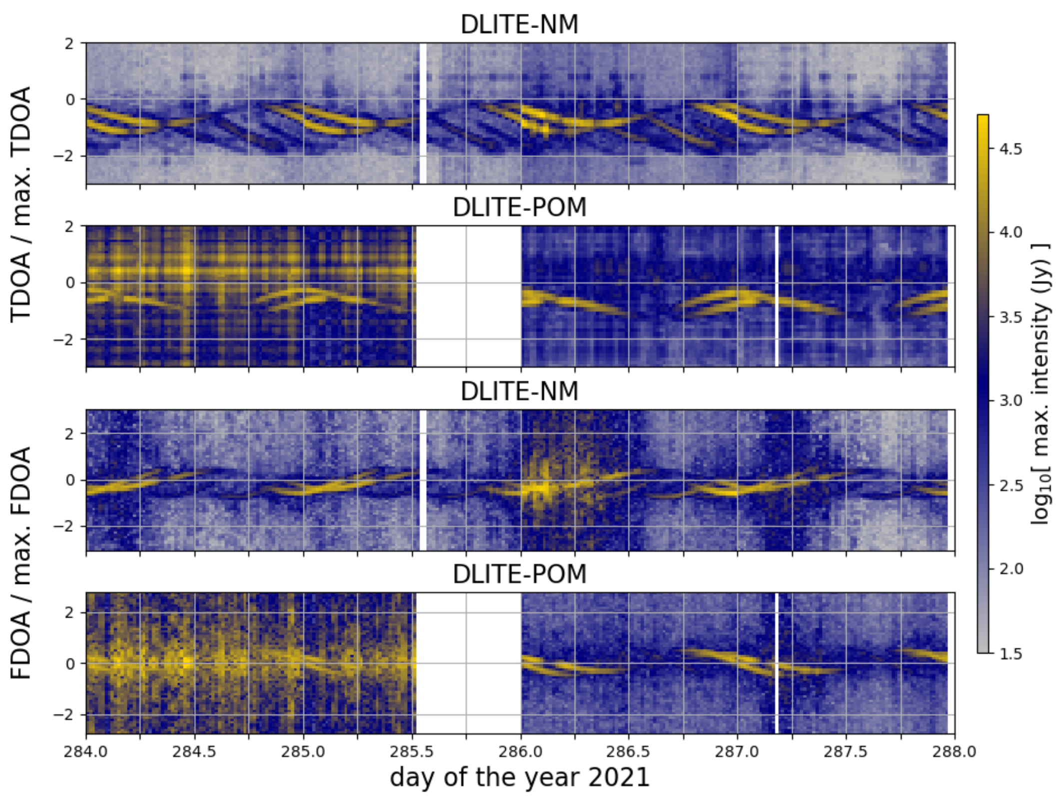

Figure 4. Peak intensity as a function of time and (upper) TDOA and (lower) FDOA for the longest baselines of DLITE-NM and DLITE-POM for 11–14 Oct. 2021.

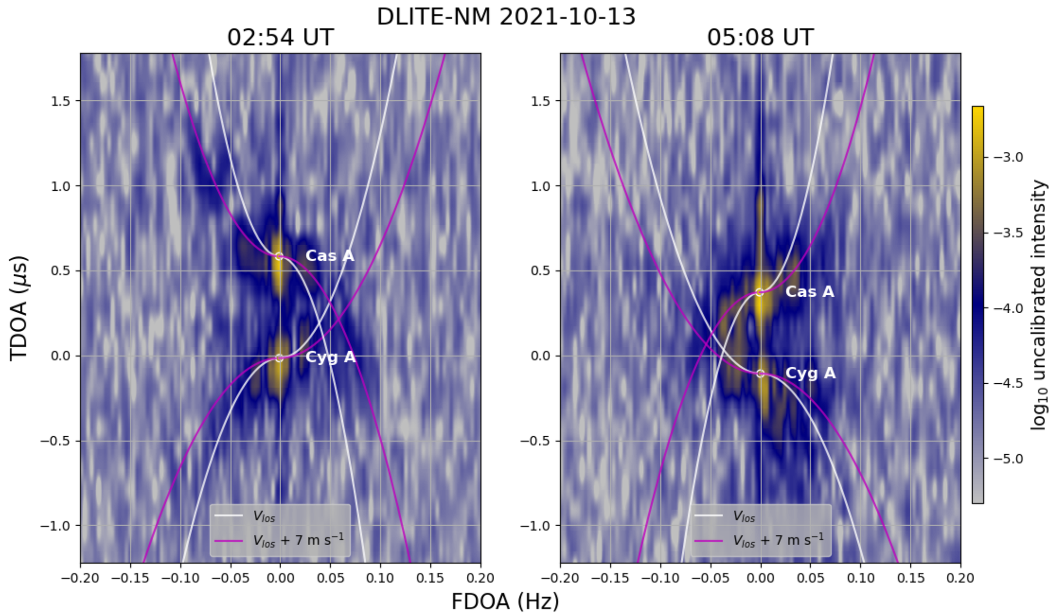

Figure 5. Using 1-s data from the longest baseline of DLITE-NM, the intensity as a function of delay and fringe rate at (left) 02:54 and (right) 05:08 UT on 13 Oct. 2021. The locations of Cyg A and Cas A are indicated with white circles. The white parabolas are the expected patterns for stationary irregularities that appear to move eastward at V_{los} due to the westward motion of the line of sight. The magenta curves are the prediction if an extra 7 m s^{-1} of eastward drift is included.

on the 12$^{\text{th}}$ to implement mitigation strategies, which as one can see, greatly improved the data quality.

Individual sources are readily differentiated in TDOA at all times within the DLITE-NM data and from the 13$^{\text{th}}$ onward within the DLITE-POM data. This is mostly true along the FDOA axis as well. There is, however, a period from ∼00–12 UT on the 13$^{\text{th}}$ where significant artifacts within the DLITE-NM data make source differentiation difficult. They are still easily resolved in the TDOA direction, which is the telltale sign of scintillations (i.e., if this were from interference, both would be affected such as the 11–12 Oct. DLITE-POM data). The FDOA versus time images also show evidence of less severe but significant scintillations observed by both systems at ∼03–09 UT on the 14$^{\text{th}}$.

As the ROTI images show in Fig. 2–3, the DLITE-NM pierce point locations directly overlapped with the elevated ROTI region at the edge of the trough on the 13$^{\text{th}}$ when the extreme 35 MHz scintillations were observed. In contrast, the DLITE-POM pierce points were located just to the north of this region and show no such evidence of elevated scintillations. This indicates that the relative narrowness of the elevated ROTI region is likely also true for the area afflicted with 35-MHz scintillations. Whether or not the spread-F region is similarly narrow is difficult to assess since the digisondes within the trough had virtually no usable signal, and the only system south of the trough edge was $\gtrsim 10°$ from it in Puerto Rico.

Given the relatively extreme nature of the scintillations observed by DLITE-NM on the 13$^{\text{th}}$, there is additional information about the irregularities that can be gleaned from a more detailed examination of the shape of the FDOA artifact. As illustrated by Fallows et al. (2014) with similar data collected with part of the Low Frequency Array

(LOFAR) telescope in the arctic region, strong scintillations will cause parabolic artifacts in the TDOA versus FDAO plane. The shapes of these depend on the projection of the observed irregularity velocity perpendicular to the line of sight, which includes the westward motion of the line of sight itself (i.e., even stationary irregularities will appear to move eastward). The DLITE TDOA, FDOA images are nominally made with data that have sampling intervals of 1 min., which is not high enough to facilitate such analysis since the parabolic shape typically only manifests for $|\mathrm{FDOA}| \gtrsim 0.05$ Hz, i.e., well above the 1-min. Nyquist limit of 0.0083 Hz. The array, however, outputs correlated data, called "visibilities," with a coherent integration time of 1 s, which are averaged to 1 min. after flagging for narrow-band and/or short duration instances of interference.

To explore the data further, the 1-s visibilities were reprocessed to produce TDOA, FDOA images every ∼5 min. This is too short to resolve Cyg A and Cas A in FDOA, but during the extreme scintillations observed on 13 Oct., they were well resolved in TDOA from the point of view of the longest DLITE-NM baseline. Two example image at around 03 and 05 UT that exhibit evidence of parabolic structures associated with both sources are shown in Fig. 5. The parabolas are patchy and lopsided, which is entirely consistent with what was observed with LOFAR by Fallows et al. (2014). The white curves show the expected parabolas if the irregularities are stationary and appear to move eastward because of the westward motion of the line of sight at V_{los}. Only one half of each parabola is plotted to prevent the plot from being overly crowded. V_{los} was calculated for an irregularity height of 300 km, which for Cyg A was 17 and 21 m s^{-1} at 03 and 05 UT, respectively. For Cas A, the values were 13 and 12 m s^{-1}. The white curves provide a reasonably good fit to Cyg A at both times. For Cas A, however, an extra 7 m s^{-1} of eastward motion is needed to reproduce what was observed, which is represented by magenta curves in Fig. 5. This could technically be the result of the assumed irregularity height of 300 km being too small. However, it would have to be increased to 475 km to fully account for the disparity, which is likely too high for the bulk of the irregularities.

The differences in observed irregularity speed between the Cyg A and Cas A lines of sight are more likely to be the result of their different positions on the sky. At both times shown in Fig. 5, Cyg A was in the western part of the sky at azimuths (clockwise from north) of about $-60°$; Cas A was in the north/northeast with azimuths ∼0°–30°. Both sources were at elevations of ∼60°. Thus, if the irregularities were drifting eastward at ∼7 m s^{-1}, this would have less of an impact on the Cyg A observations, being closer to parallel to its line of sight. To be a bit more specific, the dot products of the horizontal components of the line of sight unit vectors for the two sources are near zero (−0.001 and 0.1 at 03 and 05 UT, respectively). This implies that a plausible scenario is one in which the irregularities were drifting at ∼7 m s^{-1} to the southeast at a bearing of ∼120° (i.e., anti-parallel to the Cyg A line of sight).

2.2 The View from Space

To obtain further insight into the nature of the 12–13 Oct. mid-latitude trough and the irregularities associated with it, data from the Swarm and Ionospheric Connection Explorer (ICON) satellites were analyzed. The Swarm constellation made multiple nighttime passes over the North American region during 11–14 Oct. 2021 timeframe. The left columns of Fig. 6 show the electron density measured by each Swarm satellite's Langmuir probe as a function of latitude during one nighttime pass per day within this period. The median longitude and universal time for each pass is printed above the corresponding panel. These measurements were made in the topside at altitudes of ∼450–500 km.

These plots show a similar pattern as suggested by the TEC and bottom-side data shown in Fig. 1. Specifically, a trough appears just below 50° latitude on the 12$^{\text{th}}$ and moves equatorward on the 13$^{\text{th}}$ where it has a very sharp boundary near 30° latitude,

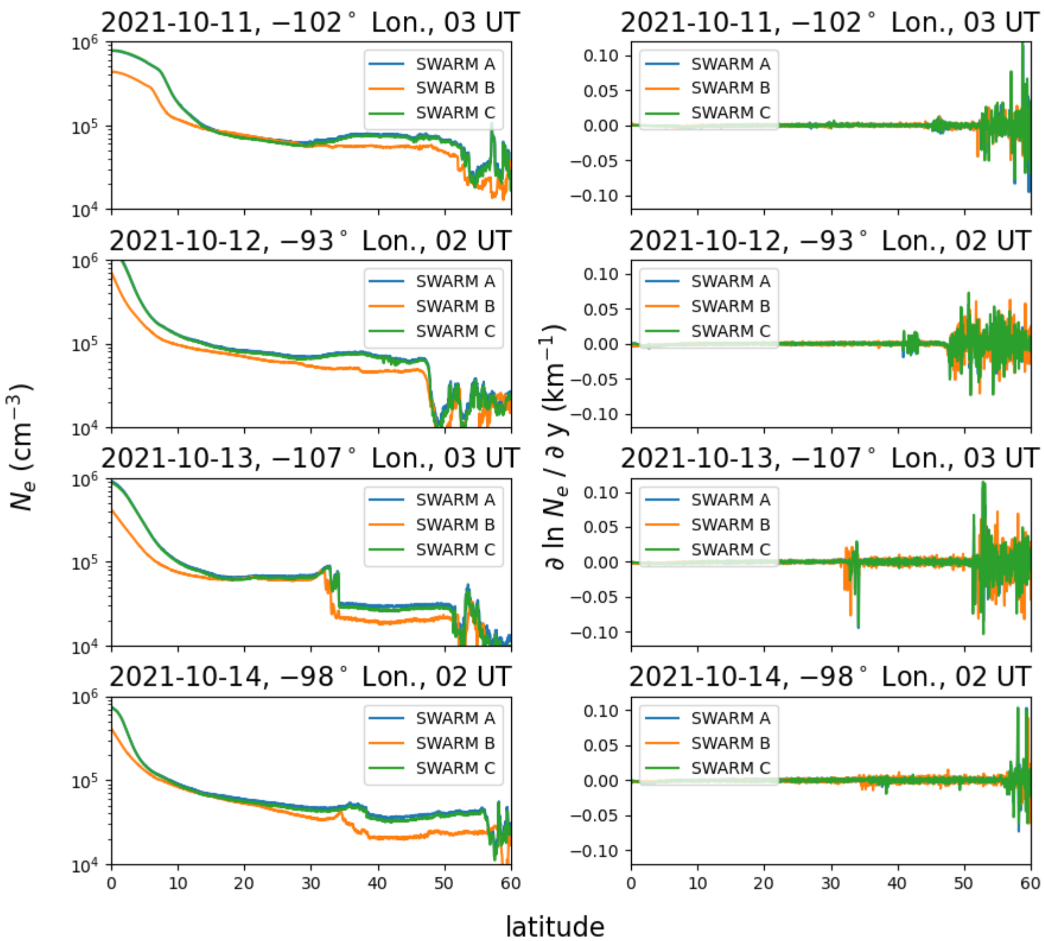

Figure 6. Left column: From 11–14 Oct. 2021, electron densities measured with the SWARM satellites at altitudes of $\sim$450–500 km during nighttime passes over North America. Right column: The spatial derivative along the path of the satellite of $\ln N_e$ (i.e., the reciprocal of the density gradient scale length) for each pass shown in the corresponding panel on the left.

which all but disappears by the 14$^{\text{th}}$. The spatial derivative of $\ln N_e$ along each satellite's poleward path is shown in the panels on the right, which is the reciprocal of the density scale length in that direction. One can see that this reaches a minimum near the southern boundary of the trough on the 13$^{\text{th}}$ with a value of $\sim$0.05–0.1 km^{-1} in the equatorward direction, or a scale length of $\sim$10–20 km.

To specifically examine structures on smaller scales, a portion of the Swarm N_e was examined close to the steep drop-off near the trough boundary on the 13$^{\text{th}}$. This is shown in the upper panel of Fig. 7, which shows N_e as a function of latitude again for the three Swarm satellites, but zoomed in near the edge of the trough. A Fourier transform was performed for each satellite in the region 32°–34.5° latitude, which is highlighted in color in the upper panel of Fig. 7. The resulting power spectra are plotted in the lower panel and are reasonably well fit by nearly a single power law over $\sim$1.5 decades in spatial frequency/wavelength. The black curve shows the case for a Kolmogorov-like turbulent spectrum with an outer scale of 200 km, which matches the spectra quite well.

As suggested in Sec. 1, the extreme density gradient near the edge of the trough suggests that a mechanism such as the GDI could be driving irregularity formation. For this to be the case, the ion velocity relative to that of the neutral gas must be in the direction of the density gradient, which is predominantly southward in this case. Mathematically, this can be expressed in the form of an approximate one-dimensional GDI growth rate $\gamma_0 = V_L/L$, where V_L is the projection of the ion velocity relative to the neutral velocity in the direction of the N_e gradient and L is the N_e scale length in that direction (Sojka et al., 1998). Thus, the growth rate is large if L is small and/or V_L is large. The Swarm Langmuir probe data imply that on the 13$^{\text{th}}$, $L \simeq 10$–20 km, which is relatively small.

In this case, the quantity V_L can be large due to high southward ion drifts and/or strong northward neutral winds. To explore these possibilities, data from the ICON satellite's Ion Velocity Meter (IVM) and Michelson Interferometer for Global High-resolution Thermospheric Imaging (MIGHTI) were obtained. During the night of the 13$^{\text{th}}$, the closest IVM F-region ion drift measurements to North America were near 25°N, 150°W at an altitude of $\sim$580 km. These showed drifts of $\sim$30 m s^{-1} toward the southwest (bearing of around $-165°$), which is not particularly large but is in the right direction for the GDI. The DLITE data presented in Sec. 2.1 implied drifts over New Mexico of $\sim$7 m s^{-1} and likely toward the southeast, which are also in the right approximate direction but even smaller.

In contrast to the regional ion drifts, the F-region neutral winds measured by MIGHTI were relatively large, $\sim$100-200 m s^{-1}, and northward. This is shown in Fig. 8 where wind vectors from nighttime passes of ICON over the region are plotted for an altitude of 301 km (red arrows) with ROTI maps computed using the entire approximate nighttime interval of 00–12 UT for 11-14 Oct. 2021. One can see that the winds point almost directly perpendicular to the elevated ROTI regions at the trough edge on 12 and 13 Oct. and in the opposite direction of the N_e gradient (i.e., roughly northward). This puts V_L at around 150 m s^{-1}, which, when combined with the Swarm data, implies $\gamma_0 \approx 0.01$ s^{-1} or a time scale of $\sim$100 s.

The N_e power spectrum shown in Fig. 7 is consistent with the spectrum of a turbulent cascade that could be driven by the GDI. With a unique combination of GPS and DLITE data, we can test how well this turbulent approximation explains the irregularities observed by these sensors. As described by Helmboldt et al. (2021), DLITE scintillation measurements are converted to measurements of the C_kL index assuming a Kolmogov spectrum. This is essentially an extrapolation from the 35-MHz Fresnel scale that dominates DLITE-observed scintillations to a scale of 1 km at which C_kL acts as a normalization factor for the full fluctuation spectrum. At a distance of a few hundred km, this Fresnel scale is $\sim$2 km, and so this is not a particularly extreme extrapolation.

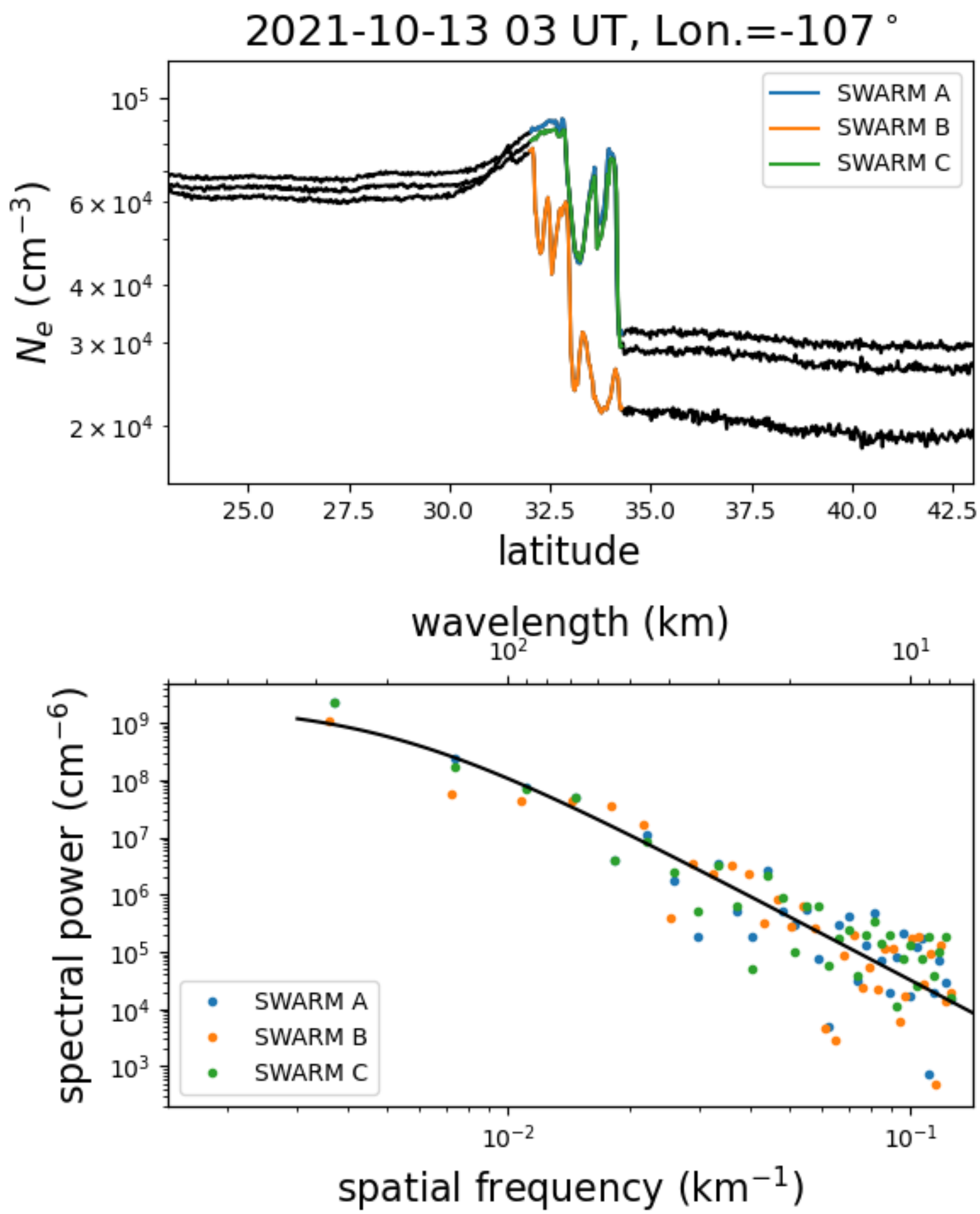

Figure 7. Upper: The electron density time series from the SWARM satellites on 13 Oct. 2021 shown in the left panels of Fig. 6, but with the region of the steep density gradient highlighted. Lower: The fluctuation spectra of the highlighted regions in the upper panel. The black curve is a fit of a power law with a Kolmogorov-like slope and an outer scale of 200 km.

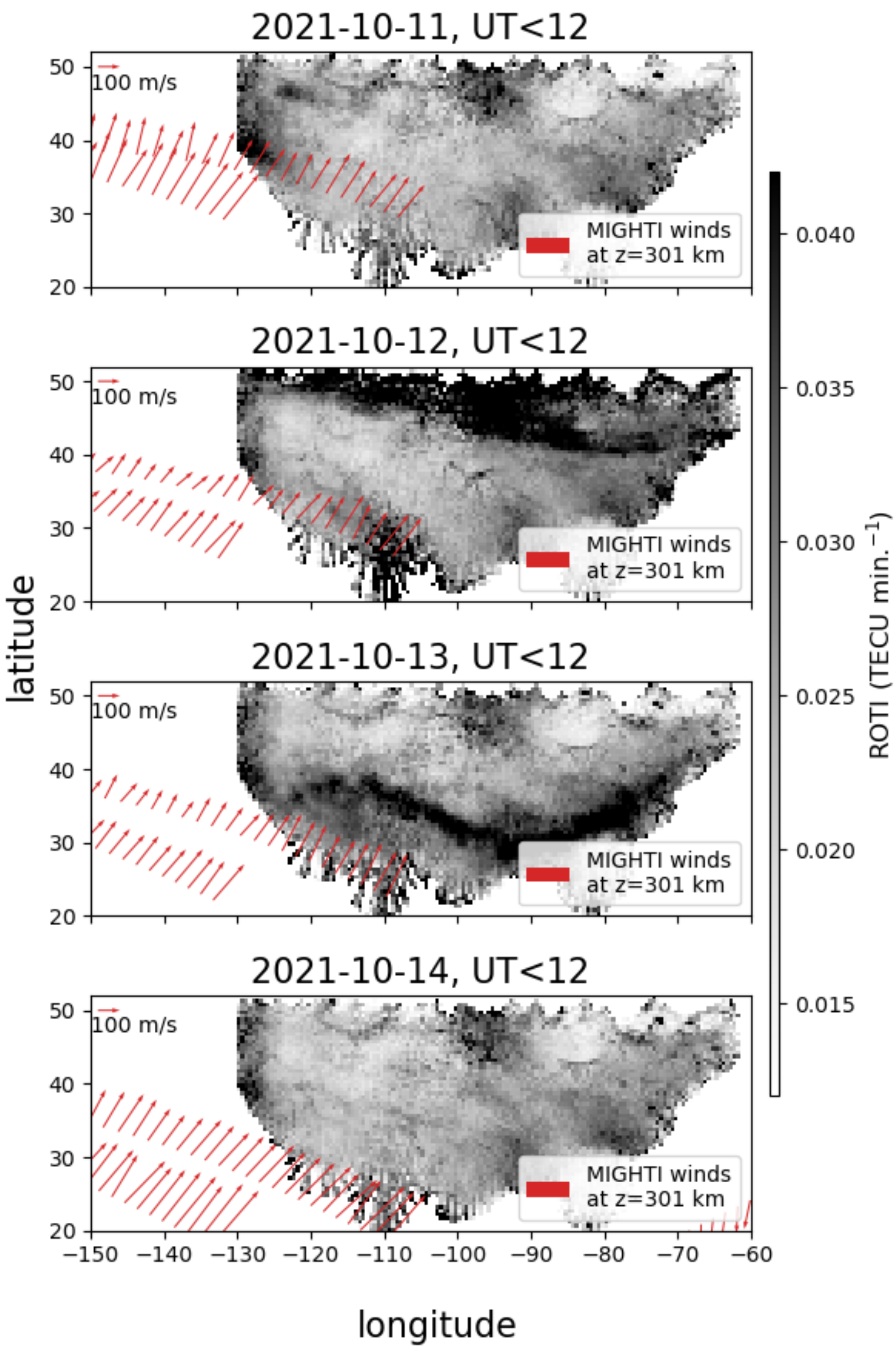

Figure 8. Neutral winds (red vectors) at a height of 301 km from the MIGHTI instrument onboard the ICON satellite from 11–14 Oct. 2021 with maps of ROTI averaged over the full 00–12 UT range.

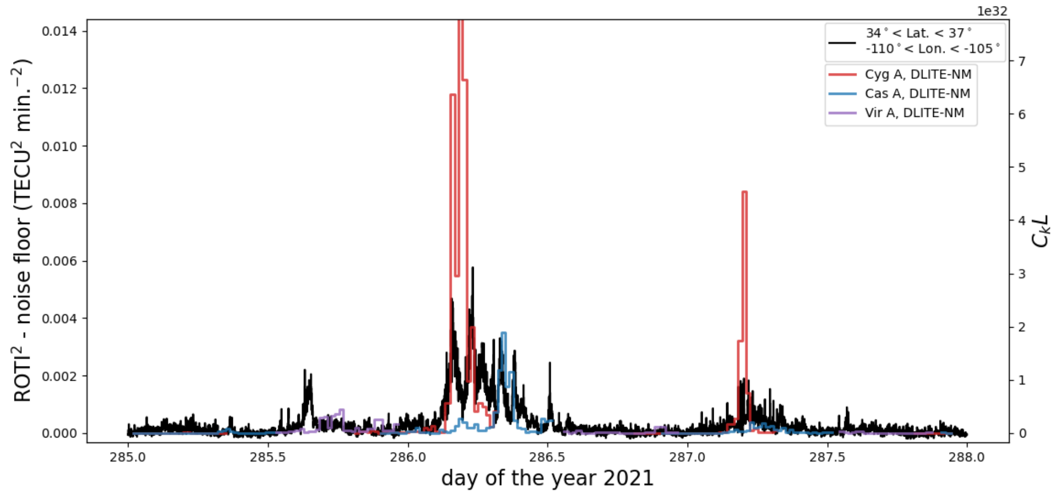

Figure 9. For 12–14 Oct. 2021, a time series of ROTI^2 averaged within the region $34° <$ Lat.$<$ $37°$ and $-110° <$ Lon. $< -105°$ at a resolution of one minute (black curve) meant to overlap with the region covered by the DLITE-NM pierce points toward Cyg A and Cas A. A median noise floor value of 4×10^{-4} TECU^2 min.$^{-2}$ has been subtracted. Values for C_kL derived from the DLITE-NM data are plotted in red and blue for Cyg A and Cas A, respectively, which follow the ordinate on the right. The two ordinates match for the median estimated conversion factor between ROTI^2 in units of TECU^2 min.$^{-2}$ and C_kL of 5.4×10^{34}. The maximum C_kL for Cyg A, which is outside the plot window, is 1×10^{34}.

In contrast, ROTI is sensitive to the integrated impact of the entire irregularity spectrum up to the largest scales measurable with the data. As Carrano et al. (2019) showed, ROTI can be converted to C_kL and vice versa but again, a power law spectrum was assumed. An examination of the geometry of the CONUS GPS observations used to make the ROTI maps combined with the conversion given by Carrano et al. (2019) and an assumed Kolmogorov-like spectral index gives a median conversion factor from from ROTI^2 in units of TECU^2 min.$^{-2}$ to C_kL of $5.4{\times}10^{34}$. In Fig. 9, a time series of ROTI^2 at one-minute resolution within the region between $34°$ and $37°$ latitude and $-110°$ and $-105°$ longitude is plotted. This region was chosen to encompass the area traversed by the pierce points of the lines of sight from DLITE-NM toward Cyg A and Cas A for elevations $>20°$. A median noise floor of $4{\times}10^{-4}$ TECU^2 min.$^{-2}$ was subtracted to approximately correct for noise biasing.

For comparison, time series of C_kL calculated with DLITE-NM scintillation data for Cyg A (red) and Cas A (blue) are also plotted and follow a separate ordinate to the right. The two ordinates are scaled such that the curves will match for the median conversion factor given above. Values of C_kL for a third source, Virgo A (Vir A), are also plotted (in purple) to provide 24 hours of coverage per day. While Vir A is several times fainter than Cyg A or Cas A, it is still bright enough to typically exhibit scintillations significantly above the system noise (Helmboldt et al., 2021), and it is visible at times when the other two are not. One can see that while there is not a one-to-one correspondence between ROTI^2 and DLITE-derived C_kL, elevated ROTI often coincides with larger C_kL values, especially during the active periods on 13 and 14 Oct.

Additionally, there are significant differences between the values for Cyg A and Cas A, which typically differ by a factor of $\sim$2 (Helmboldt et al., 2021), but are as much as 100 times different in this case (the maximum C_kL for Cyg A was $1{\times}10^{34}$ and is outside the plot window of Fig. 9). This indicates a relatively patchy distribution of irregularities that likely drives down ROTI^2, which is averaged over a significant area. This patchiness also likely contributes to the temporal variability of ROTI^2, which shows multiple peaks on 13 Oct. that are spaced by ∼1 hour from one another. Based on DLITE and IVM data, the irregularities were drifting at ∼7–30 m s^{-1}, implying that the 1-hour quasi-periodic ROTI structure could be from patches spaced by ∼25–110 km. The sometimes substantial differences between Cyg A and Cas A are consistent with this given that their pierce points were separated by ∼220 km.

3 Conclusions

The combination of ground- and space-based data presented here paint a relatively clear picture of irregularity formation along the edge of a storm-induced mid-latitude trough over North America in Oct. 2021. The trough begins to appear at high latitudes on the 11$^{\text{th}}$ as the Dst index begins to decrease. At the onset of the storm on the 12$^{\text{th}}$ when Dst reaches a minimum, the trough begins to move equatorward and the impact of irregularities at the edge of the trough become apparent within GPS data as increased ROTI. By the 13$^{\text{th}}$, the edge of the trough had become very sharply defined and descended down to ∼30° latitude. There, irregularities within a relatively narrow strip (∼5° wide) along the boundary caused inflated ROTI, strong 35 MHz scintillations observed from New Mexico, and spread-F within the ionograms from multiple digisonde stations. While the electron density and TEC remained relatively depleted on the 14$^{\text{th}}$, the sharp equatorward edge and its associated irregularities were gone by this time.

Spaced-based measurements of F-region N_e and neutral winds revealed that near the trough edge, conditions for the GDI were optimal with an e-folding growth time of about 100 s. The power spectrum of N_e fluctuations near the boundary region was consistent with a turbulent cascade with an outer scale of about 200 km. Comparisons of ROTI measurements near New Mexico with C_kL values derived from 35 MHz scintillations were also roughly consistent with the assumption of a Kolmogorov-like spectrum, albeit with a relatively patchy spatial distribution of irregularities. The detailed structure of scintillation-induced artifacts within 35 MHz images of cosmic radio sources from New Mexico on the 13$^{\text{th}}$ also revealed that the irregularities were moving relatively slowly, ∼7 m s^{-1}, likely in the southeast direction. During this time, the trough edge remained relatively stable for several hours, and it appears the irregularities that formed there did not stray far over that time.

While limited conclusions can be drawn from a single case study, these result can provide motivation for follow-up investigations of the role the GDI plays in irregularity formation near mid-latitude troughs. This hypothesis is highly testable as one would only expect irregularities to form near a well-defined edge if the neutral winds and/or ion drifts were strong and pointed in the optimal direction(s). This is particularly relevant to forecasting of strong mid-latitude irregularities that are much smaller than the typical grid size of global or even regional ionospheric models. If the GDI is a primary driver and if such models can accurately predict trough formation and evolution, then the GDI growth rate can be calculated from simulated data and an irregularity probability may be estimated. For instance, Huba and Liu (2020) used a combination of space-based data and high-resolution simulations to show that the in the equatorial region, the generalized Rayleigh-Taylor instability growth rate was a good indicator of the likelihood of plasma bubble formation. However, achieving something similar with trough-driven irregularities at mid-latitudes would require a foundation of empirical data to quantify the likelihood of irregularity formation for a given GDI growth rate. Hence, such follow-up statistical studies may be of great interest.

Independent of any future follow-on work, this study stands as a unique look into a relatively well-known phenomenon. By combining several different remote sensing and in situ measurements surrounding the 12 Oct. 2021 geomagnetic storm, the mid-latitude trough was shown to be an effective engine for the formation of irregularities that wreak havoc on radio frequency systems from frequencies of a few MHz to 1.5 GHz.

Acknowledgments

Derived DLITE data products used within this publication are available at `https://lda10g.alliance.unm.edu/~dlite`. Development and testing of the DLITE system were supported by the Defense Advanced Research Agency (DARPA) Space Environment Exploitation (SEE) program. GPS RINEX data were obtained from the IGS (`https://cddis.nasa.gov`), CORS (`https://www.ngs.noaa.gov/CORS/data.shtml`), SOPAC (`http://garner.ucsd.edu`), and UNAVCO (`https://www.unavco.org/data/data.html`) databases. Vertical TEC data were obtained from the Madrigal database at `http://millstonehill.haystack.mit.edu`. Digisonde data were obtained from the Global Ionosphere Radio Observatory (`http://giro.uml.edu`). Geomagnetic indices were obtained from the NASA OMNIWeb Plus service (`https://omniweb.gsfc.nasa.gov`). Swarm data were obtained from `https://swarm-diss.eo.esa.int`. ICON data from the IVM and MIGHTI instruments were obtained from FTP servers with links given at `https://icon.ssl.berkeley.edu/Data/Data-Product-Matrix`.

References

Carrano, C. S., Groves, K. M., & Rino, C. L. (2019). On the relationship between the rate of change of total electron content index (roti), irregularity strength (ckl), and the scintillation index (s4). *Journal of Geophysical Research: Space Physics*, *124*(3), 2099-2112. Retrieved from `https://agupubs.onlinelibrary.wiley.com/doi/abs/10.1029/2018JA026353` doi: https://doi.org/10.1029/2018JA026353

Fallows, R. A., Coles, W. A., McKay-Bukowski, D., Vierinen, J., Virtanen, I. I., Postila, M., … Stuurwold, K. (2014). Broadband meter-wavelength observations of ionospheric scintillation. *Journal of Geophysical Research: Space Physics*, *119*(12), 10,544-10,560. Retrieved from `https://agupubs.onlinelibrary.wiley.com/doi/abs/10.1002/2014JA020406` doi: https://doi.org/10.1002/2014JA020406

Foster, J. C., Erickson, P. J., Coster, A. J., Goldstein, J., & Rich, F. J. (2002). Ionospheric signatures of plasmaspheric tails. *Geophysical Research Letters*, *29*(13), 1-1-1-4. Retrieved from `https://agupubs.onlinelibrary.wiley.com/doi/abs/10.1029/2002GL015067` doi: https://doi.org/10.1029/2002GL015067

Helmboldt, J. F., Markowski, B. B., Bonanno, D. J., Clarke, T. E., Dowell, J., Hicks, B. C., … Taylor, G. B. (2021). The deployable low-band ionosphere and transient experiment. *Radio Science*, *56*(7), e2021RS007298. Retrieved from `https://agupubs.onlinelibrary.wiley.com/doi/abs/10.1029/2021RS007298` (e2021RS007298 2021RS007298) doi: https://doi.org/10.1029/2021RS007298

Helmboldt, J. F., & Zabotin, N. (2022). An observed trend between mid-latitudes km-scale irregularities and medium-scale traveling ionospheric disturbances. *Radio Science*, *57*(5), e2021RS007396. Retrieved from `https://agupubs.onlinelibrary.wiley.com/doi/abs/10.1029/2021RS007396` (e2021RS007396 2021RS007396) doi: https://doi.org/10.1029/2021RS007396

Hicks, B. C., Paravastu-Dalal, N., Stewart, K. P., Erickson, W. C., Ray, P. S., Kassim, N. E., … Weiler, K. W. (2012, October). A Wide-Band, Active Antenna System for Long Wavelength Radio Astronomy. *Publications of the Astronomical Society of the Pacific*, *124*, 1090-1104. doi: 10.1086/668121

Huba, J. D., & Liu, H.-L. (2020). Global modeling of equatorial spread f with sami3/waccm-x. *Geophysical Research Letters*, *47*(14), e2020GL088258.

Retrieved from https://agupubs.onlinelibrary.wiley.com/doi/abs/10.1029/2020GL088258 (e2020GL088258 10.1029/2020GL088258) doi: https://doi.org/10.1029/2020GL088258

Krankowski, A., Shagimuratov, I. I., Ephishov, I. I., Krypiak-Gregorczyk, A., & Yakimova, G. (2009, June). The occurrence of the mid-latitude ionospheric trough in GPS-TEC measurements. *Advances in Space Research*, *43*(11), 1721-1731. doi: 10.1016/j.asr.2008.05.014

Ledvina, B. M., Makela, J. J., & Kintner, P. M. (2002). First observations of intense gps l1 amplitude scintillations at midlatitude. *Geophysical Research Letters*, *29*(14), 4-1-4-4. Retrieved from https://agupubs.onlinelibrary.wiley.com/doi/abs/10.1029/2002GL014770 doi: https://doi.org/10.1029/2002GL014770

Linson, L. M., & Workman, J. B. (1970). Formation of striations in ionospheric plasma clouds. *Journal of Geophysical Research (1896-1977)*, *75*(16), 3211-3219. Retrieved from https://agupubs.onlinelibrary.wiley.com/doi/abs/10.1029/JA075i016p03211 doi: https://doi.org/10.1029/JA075i016p03211

Rodrigues, F. S., Socola, J. G., Moraes, A. O., Martinis, C., & Hickey, D. A. (2021). On the properties of and ionospheric conditions associated with a mid-latitude scintillation event observed over southern united states. *Space Weather*, *19*(6), e2021SW002744. Retrieved from https://agupubs.onlinelibrary.wiley.com/doi/abs/10.1029/2021SW002744 (e2021SW002744 2021SW002744) doi: https://doi.org/10.1029/2021SW002744

Schunk, R. W., Banks, P. M., & Raitt, W. J. (1976, July). Effects of electric fields and other processes upon the nighttime high-latitude F layer. *Journal of Geophysical Research*, *81*(19), 3271. doi: 10.1029/JA081i019p03271

Shinbori, A., Otsuka, Y., Tsugawa, T., Nishioka, M., Kumamoto, A., Tsuchiya, F., … Nishitani, N. (2018). Temporal and spatial variations of storm time midlatitude ionospheric trough based on global gnss-tec and arase satellite observations. *Geophysical Research Letters*, *45*(15), 7362-7370. Retrieved from https://agupubs.onlinelibrary.wiley.com/doi/abs/10.1029/2018GL078723 doi: https://doi.org/10.1029/2018GL078723

Sojka, J. J., Subramanium, M. V., Zhu, L., & Schunk, R. W. (1998, November). Gradient drift instability growth rates from global-scale modeling of the polar ionosphere. *Radio Science*, *33*(6), 1915-1928. doi: 10.1029/98RS02490

Irregularities observed at the edge of a mid-latitude ionospheric trough following a geomagnetic storm

J. F. Helmboldt[1]

[1]US Naval Research Laboratory, 4555 Overlook Ave. SW, Washington, DC 20375, USA.

Key Points:

- A multitude of ground- and space-based sensors were used to study a storm-induced trough, its evolution, and its impact over North America.
- Irregularities at the equatorward edge of the trough impacted radio frequency systems from a few MHz to 1.5 GHz.
- Space-based in situ and remote sensing data point to the gradient drift instability as the most likely driver of irregularity formation.

Corresponding author: J. F. Helmboldt, joseph.helmboldt@nrl.navy.mil

Abstract

This manuscript presents the analysis of data from multiple ground- and space-based sensors in the North American region before, during, and after the 12 Oct. 2021 geomagnetic storm. The data show the formation and equatorward propagation of a density trough, which manifested within bottom-side and top-side electron density data as well as within maps of total electron content (TEC). During the recovery phase on the 13$^{\text{th}}$, the equatorward edge of the trough settled at around 30° latitude and exhibited a steep density gradient. By the 14$^{\text{th}}$, this sharp boundary had disappeared. Near this edge on the 13$^{\text{th}}$, small-scale irregularities formed. The impact of these was observed within Global Positioning System (GPS) data as elevated rate of TEC index (ROTI) and presented as strong 35 MHz scintillations of cosmic radio sources as well as spread-F within ionograms from multiple digisonde systems. GPS and 35-MHz data demonstrated that the irregularity region was narrowly confined ($\lesssim$5° wide) near the trough edge. The 35-MHz scintillation data also showed that the irregularities were moving relatively slowly at $\sim$7 m s^{-1}, likely toward the southeast. Density and velocity measurements demonstrate that the conditions near the trough boundary we highly favorable for the gradient drift instability (GDI) with the one-dimensional growth rate estimated to be $\sim$0.01 s^{-1}. Since these conditions persisted for many hours, this growth rate was more than sufficient for the GDI to be considered the primary driver of irregularity formation in this case.

Plain Language Summary

Earth's ionosphere, the ionized portion of the upper atmosphere, is a dynamic environment, often beset with irregularities and disturbances that interfere with radio frequency signals that travel through it. In this regard, mid-latitudes are usually quite tame relative to the equatorial and polar regions. However, when significant geomagnetic disturbances, or "storms," occur, this normally placid region can become anything but. This paper presents the results of a study that examines the impact of a storm over North America, using several space- and ground-based sensors. Of particular interest is the formation of a density trough that moves toward the equator after the onset of the storm. Multiple sensors show evidence of this trough and still others show a preponderance of small-scale irregularities (on the order of 100 meters to a few kilometers) near its southern boundary. A holistic analysis indicates that these irregularities are consistent with a turbulent cascade moving relatively slowly, likely toward the south or southeast. Conditions near the trough were observed to be conducive with the so-called gradient drift instability. This is known to be a primary driver of irregularity formation within other settings, and appears to be the culprit in this case as well.

1 Introduction

At mid-latitudes, Earth's ionosphere is generally a quiet and uneventful environment when compared to the more active and dynamic settings of the equatorial and arctic/auroral regions. There are, of course, exceptions to this general statement, especially under geomagnetic storm conditions. These events erode the plasmasphere and initiate plume formation, leading to storm enhanced densities (SEDs) at mid-latitudes with telltale morphologies (Foster et al., 2002). This is related to a strong sub-auroral polarization stream (SAPS), which also leads to the formation of a density trough. This trough results from an increase in the recombination rate in the F-region due to an enhancement in ion-neutral heating related to the strong SAPS electric field (Schunk et al., 1976).

Generally, during geomagnetically active periods, such density troughs have been observed to move equatorward and to have a relatively sharp boundary on the equatorial edge (Krankowski et al., 2009; Shinbori et al., 2018). The combination of these two factors implies that near this edge, the conditions could be ripe for the formation of irregularities that are unusually strong for mid-latitudes via, e.g., the gradient drift instability (GDI; Linson and Workman (1970)). Indeed, isolated incidences of intense microwave-frequency scintillations have been observed with specialized Global Positioning System (GPS) ground-based sensors at mid-latitudes near an equatorward-propagating trough following geomagnetic activity (Ledvina et al., 2002; Rodrigues et al., 2021).

This manuscript adds to this growing body of work with similar analysis of data collected around the geomagnetic storm that occurred on 12 Oct. 2021. In this case, a unique new instrument, the Deployable Low-band Ionosphere and Transient Experiment (DLITE; Helmboldt et al. (2021)), was used to measure scintillations at a much lower frequency, 35 MHz, from New Mexico and Maryland. These measurements combined with GPS and digisonde data as well as spacecraft observations support the conclusion that a turbulent cascade was triggered by the GDI at the edge of the trough associated with this storm. This resulted in relatively intense irregularity activity impacting radio frequency systems from frequencies of a few MHz to 1.5 GHz. The data and analysis are described below in Sec. 2 with conclusions discussed in more detail in Sec. 3.

2 Data and Analysis

2.1 The Storm and Mid-latitude Features

The storm that occurred on 12 Oct. 2021 was initiated by a coronal mass ejection, which impacted just before 02 UT. The impact actually initiated a double storm with minima in the Dst index at around 06 and 14 UT. These are evident in the upper panel of Fig. 1, which shows the Dst time series from 11 Oct. (day of the year, DOY= 284) through the end of 14 Oct. To illustrate the impact on mid-latitude electron density, vertical total electron content (TEC) maps were obtained at five-minute cadence from the Madrigal database. A keogram at a fixed longitude of $-100°$ is shown in Fig. 1 with the colormap set to highlight the nighttime ionosphere when the trough is more prevalent/obvious. As the Dst index plummets, a narrow trough appears and moves continuously equatorward during the night of 12 Oct. (DOY= 285). When the lower boundary moves below $\sim40°$ latitude, the trough broadens significantly. During the recovery phase on the night of 13 Oct. (DOY= 286), the lower trough boundary has settled at $\sim30°$ latitude and is quite sharp. By the night of 14 Oct., this clear edge has eroded substantially. Within the keogram, times of 03 and 06 UT are highlighted with green dashed lines and will be explored in more detail below.

To search for evidence of GPS scintillations/irregularities, publicly available data from over 2,000 GPS receivers in the continental United States (CONUS) were obtain in receiver independent exchange (RINEX) format and processed to look for rapid variations in TEC. These data were predominantly recorded at a cadence of 30 s. Consequently, they were used to compute the rate of TEC index (ROTI) by computing the difference in TEC between samples separated by 30 s for each satellite/receiver pair. Using pierce point locations at an altitude of 300 km and an elevation limit of $>30°$ to avoid multi-path effects, the measurements of ROTI^2 were averaged within $0.5° \times 0.5° \times 1$ min. bins in latitude/longitude/UT. To make a keogram similar to the one created for vertical TEC, these were further averaged to a cadence of 5 min. and between longitudes of $-105°$ and $-95°$. The square root of the result is shown as a ROTI keogram in Fig. 1. From this, one can see elevated ROTI at the boundary of the trough during the nights of 12 and 13 Oct.

To demonstrate the impact of the trough and its equatorward movement between 12 and 13 Oct. on electron density and not just TEC, we also show time series of the `foF2` parameter obtained from nine digisonde systems from throughout North America in the bottom panel of Fig. 1, color-coded by latitude. One can see that the lowest latitudes are not affected by the trough as they are too far south. The highest latitudes (up to $\sim45°$), however, show noticeably lower densities, especially during the night of 13 Oct.

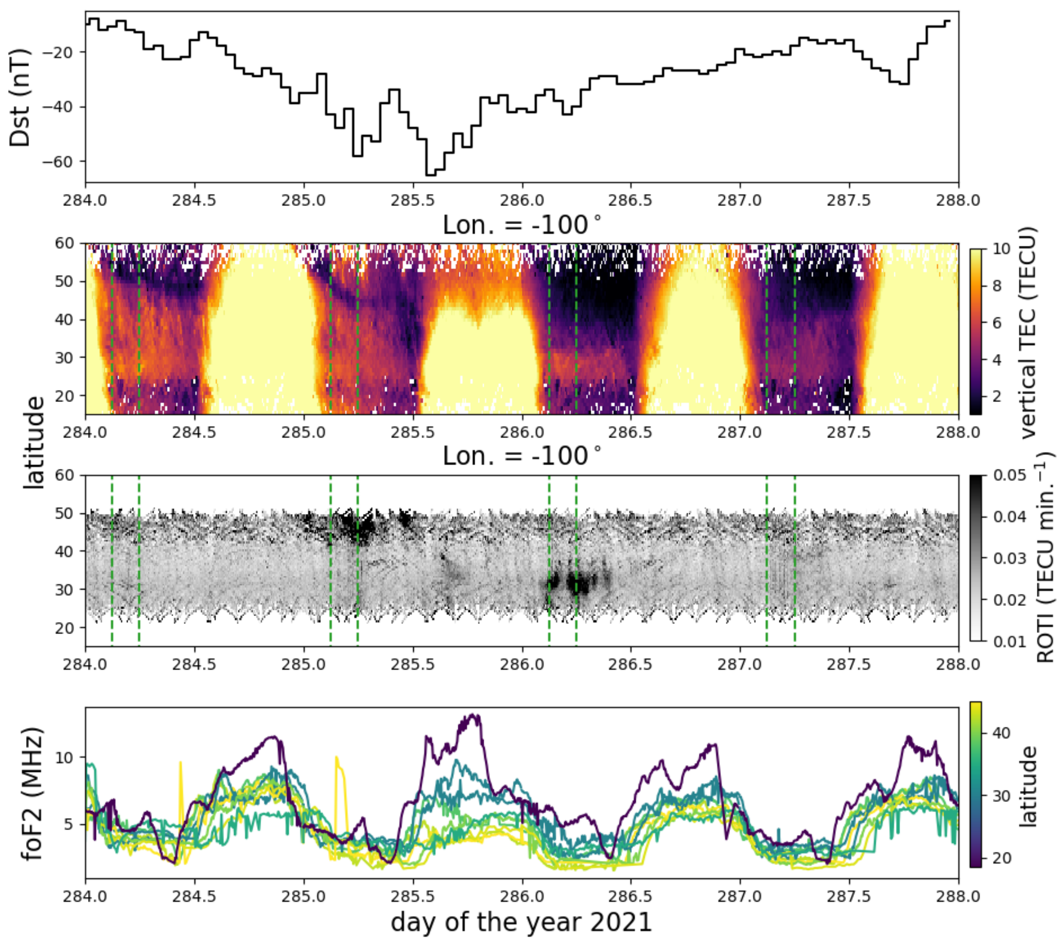

Figure 1. Plots showing the 12 Oct. 2021 storm and its ionospheric impacts. Upper: Dst index time series from 11-14 Oct. Middle: Keograms for vertical TEC and ROTI at a longitude of $-100°$; times of 03 and 06 UT that will be highlighted in subsequent figures are indicated with vertical dashed green lines. Bottom: Time series of `foF2` from nine North American digisonde systems, color coded by latitude.

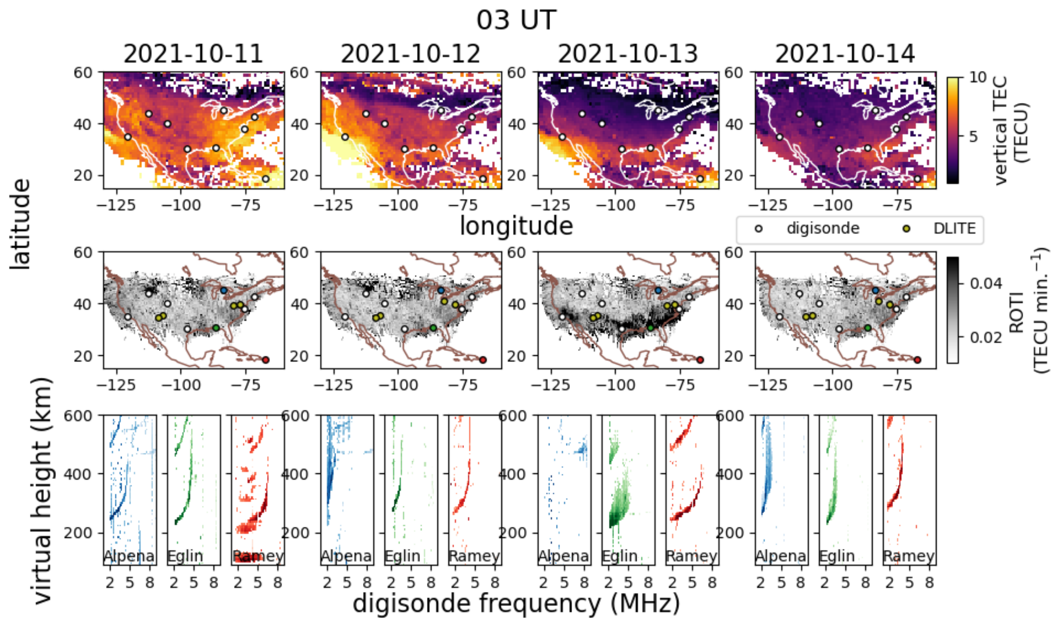

Figure 2. Upper row: For 11–14 Oct. 2021, maps of vertical TEC at 03 UT with locations of digisonde systems indicated with white points. Middle row: Maps of ROTI (one-hour bin) with digisonde locations and DLITE pierce points toward Cyg A and Cas A highlighted. Bottom row: Ionograms (O-mode only) from three example digisondes. The colormaps used correspond to the colors of the circles used to indicate the digisondes' locations in the middle row of panels.

At this time, multiple digisondes had `foF2` at the minimum frequency used (∼2 MHz), implying the ionosphere all but disappeared to those radars.

Fig. 2–3 show maps of vertical TEC and ROTI at example times of 03 and 06 UT on each date between 11 and 14 Oct. 2021. In this case, the measurements of ROTI^2 were left at a resolution of $0.5° \times 0.5°$ in latitude/longitude but were averaged within ± 30 minutes of the central time (i.e., 03 or 06 UT). The maps show the square root of the results. Within each panel, the locations of the North American digisonde systems with available data are shown with white points.

On the ROTI maps, three example digisondes are highlighted in color: Alpena, Michigan (blue); Eglin Air Force Base, Florida (green); and Ramey Air Force Base, Puerto Rico (red). Ionograms (O-mode only) from these three systems are shown below the ROTI maps for each date/time. With the exception of some interference issues, the Ramey ionograms show reasonably well defined, typical-looking traces. The Alpena ionogram shows some evidence of broadening at both 03 and 06 UT on 12 Oct. when the enhanced ROTI region was nearby and essentially disappears on the 13$^{\text{th}}$, recovering somewhat on the 14$^{\text{th}}$. The Eglin ionograms appear relatively normal except on the 13$^{\text{th}}$ when there is a substantial amount of spread-F at both 03 and 06 UT and a significant decrease in density at 06 UT. These incidences of spread-F occurred when the lower trough boundary moved over the region. Similar behavior was observed within the data for the digisonde in Austin, Texas, which was also at the trough edge on 13 Oct.

Within the ROTI maps in Fig. 2–3, yellow points indicate 300 km altitude pierce points associated with the DLITE systems operating in New Mexico (at 34.07°N, 107.63°W) and Maryland (at 38.56°N, 77.06°W). Each DLITE system is an array of four inverted vee dipole antennas designed for the Long Wavelength Array (Hicks et al., 2012). These

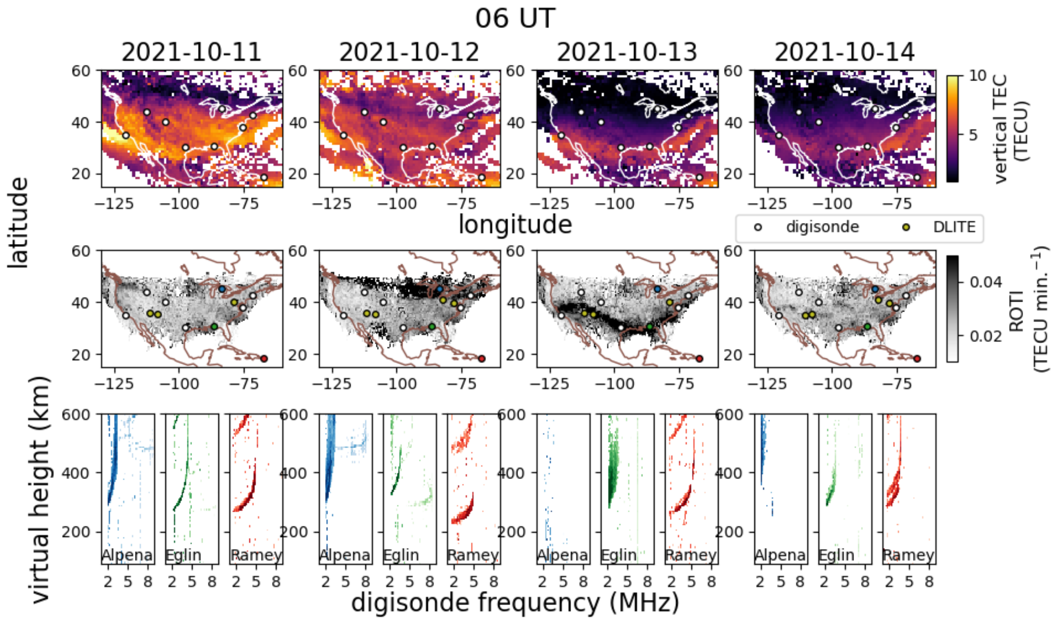

Figure 3. The same as Fig. 2, but for 06 UT.

antennas are separated from one another by ∼200–450 m and used together as an interferometric telescope. They observe the entire sky in a 30–40 MHz band, using time and frequency difference of arrival (TDOA and FDOA, respectively) methods to resolve individual cosmic radio sources from one another. There are six such sources that are bright enough to be observed with a DLITE system from the Northern Hemisphere, 2–4 of which are visible at the same time. The brightest two of these by far are Cygnus A (Cyg A) and Cassiopeia A (Cas A), which are observable together for several hours per day are are consistently the best objects to use for scintillation studies at 35 MHz. The pierce points shown in Fig. 2–3 are for these two sources.

As detailed by Helmboldt et al. (2021), the level of 35 MHz scintillations can be measured with each pair of antennas, or "baseline," by using ∼1 hour of data to make a TDOA, FDOA image of the sky. With this amount of data, sources are well resolved from one another and easily identifiable given the known antenna locations. Scintillations cause a plateau-like artifact to form in the FDOA direction only, associated with the scintillating source. The magnitude of this plateau relative to the peak observed intensity provides a means to measure the S_4 index. Such measurements can also be converted to the C_kL irregularity index, which is independent of frequency and observing geometry and is proportional to the integrated electron density variance within the irregularity region. The methods used to do this are described in detail by Helmboldt et al. (2021) and show good agreement with similar irregularity measurements made with a nearby dynasonde radar system (Helmboldt & Zabotin, 2022).

Fig. 4 shows images of the peak intensity as a function of time and either TDOA or FDOA for the longest baseline of the New Mexico system, DLITE-NM, and the system near Pomonkey, Maryland, DLITE-POM, which are from TDOA, FDOA images generated at a ∼20 min. cadence. For DLITE-NM, this is a ∼420-m east/west baseline, and for DLITE-POM, the baseline is ∼350-m north/south. One can see that prior to 13 Oct. (DOY= 286), the DLITE-POM data were quite noisy, which was due to interference from a faulty utility pole at the site (bad insulators). The array was shut down temporarily

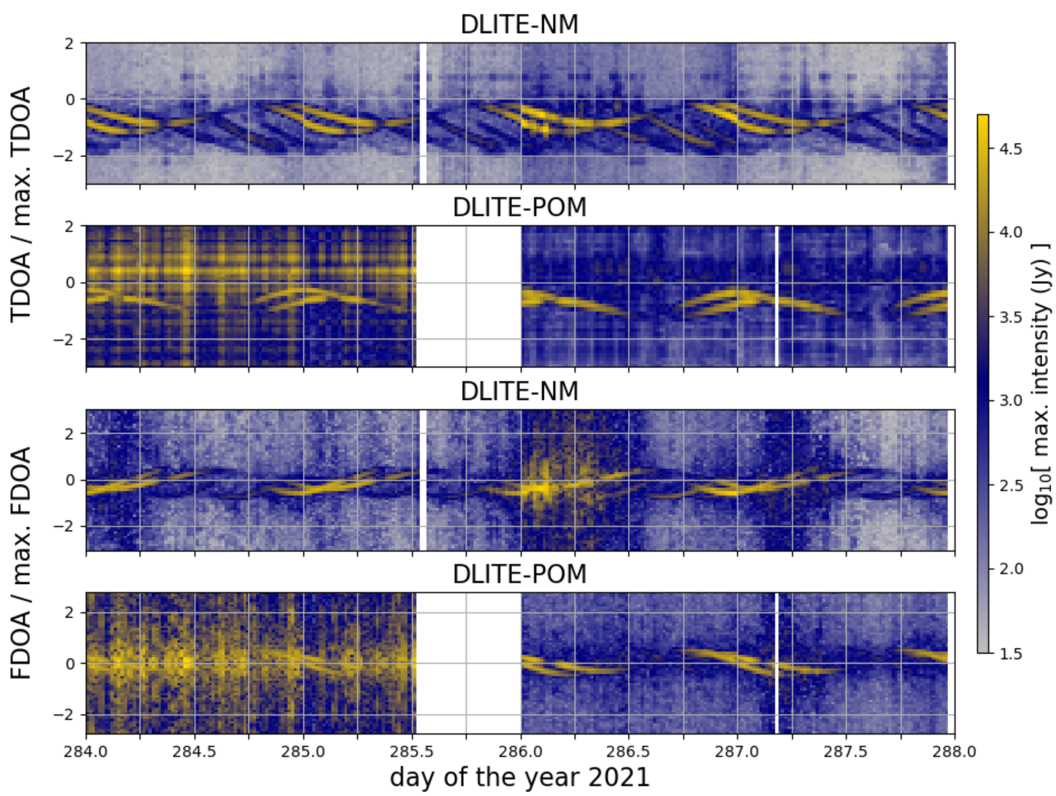

Figure 4. Peak intensity as a function of time and (upper) TDOA and (lower) FDOA for the longest baselines of DLITE-NM and DLITE-POM for 11–14 Oct. 2021.

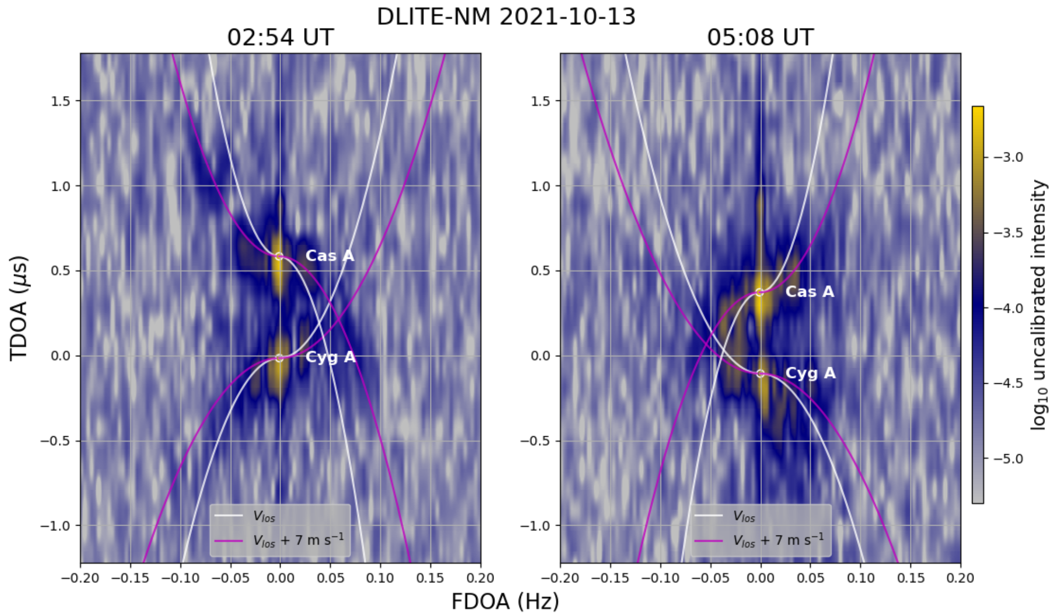

Figure 5. Using 1-s data from the longest baseline of DLITE-NM, the intensity as a function of delay and fringe rate at (left) 02:54 and (right) 05:08 UT on 13 Oct. 2021. The locations of Cyg A and Cas A are indicated with white circles. The white parabolas are the expected patterns for stationary irregularities that appear to move eastward at V_{los} due to the westward motion of the line of sight. The magenta curves are the prediction if an extra 7 m s^{-1} of eastward drift is included.

on the 12$^{\text{th}}$ to implement mitigation strategies, which as one can see, greatly improved the data quality.

Individual sources are readily differentiated in TDOA at all times within the DLITE-NM data and from the 13$^{\text{th}}$ onward within the DLITE-POM data. This is mostly true along the FDOA axis as well. There is, however, a period from ∼00–12 UT on the 13$^{\text{th}}$ where significant artifacts within the DLITE-NM data make source differentiation difficult. They are still easily resolved in the TDOA direction, which is the telltale sign of scintillations (i.e., if this were from interference, both would be affected such as the 11–12 Oct. DLITE-POM data). The FDOA versus time images also show evidence of less severe but significant scintillations observed by both systems at ∼03–09 UT on the 14$^{\text{th}}$.

As the ROTI images show in Fig. 2–3, the DLITE-NM pierce point locations directly overlapped with the elevated ROTI region at the edge of the trough on the 13$^{\text{th}}$ when the extreme 35 MHz scintillations were observed. In contrast, the DLITE-POM pierce points were located just to the north of this region and show no such evidence of elevated scintillations. This indicates that the relative narrowness of the elevated ROTI region is likely also true for the area afflicted with 35-MHz scintillations. Whether or not the spread-F region is similarly narrow is difficult to assess since the digisondes within the trough had virtually no usable signal, and the only system south of the trough edge was $\gtrsim 10°$ from it in Puerto Rico.

Given the relatively extreme nature of the scintillations observed by DLITE-NM on the 13$^{\text{th}}$, there is additional information about the irregularities that can be gleaned from a more detailed examination of the shape of the FDOA artifact. As illustrated by Fallows et al. (2014) with similar data collected with part of the Low Frequency Array

(LOFAR) telescope in the arctic region, strong scintillations will cause parabolic artifacts in the TDOA versus FDAO plane. The shapes of these depend on the projection of the observed irregularity velocity perpendicular to the line of sight, which includes the westward motion of the line of sight itself (i.e., even stationary irregularities will appear to move eastward). The DLITE TDOA, FDOA images are nominally made with data that have sampling intervals of 1 min., which is not high enough to facilitate such analysis since the parabolic shape typically only manifests for $|\mathrm{FDOA}| \gtrsim 0.05$ Hz, i.e., well above the 1-min. Nyquist limit of 0.0083 Hz. The array, however, outputs correlated data, called "visibilities," with a coherent integration time of 1 s, which are averaged to 1 min. after flagging for narrow-band and/or short duration instances of interference.

To explore the data further, the 1-s visibilities were reprocessed to produce TDOA, FDOA images every ∼5 min. This is too short to resolve Cyg A and Cas A in FDOA, but during the extreme scintillations observed on 13 Oct., they were well resolved in TDOA from the point of view of the longest DLITE-NM baseline. Two example image at around 03 and 05 UT that exhibit evidence of parabolic structures associated with both sources are shown in Fig. 5. The parabolas are patchy and lopsided, which is entirely consistent with what was observed with LOFAR by Fallows et al. (2014). The white curves show the expected parabolas if the irregularities are stationary and appear to move eastward because of the westward motion of the line of sight at V_{los}. Only one half of each parabola is plotted to prevent the plot from being overly crowded. V_{los} was calculated for an irregularity height of 300 km, which for Cyg A was 17 and 21 m s^{-1} at 03 and 05 UT, respectively. For Cas A, the values were 13 and 12 m s^{-1}. The white curves provide a reasonably good fit to Cyg A at both times. For Cas A, however, an extra 7 m s^{-1} of eastward motion is needed to reproduce what was observed, which is represented by magenta curves in Fig. 5. This could technically be the result of the assumed irregularity height of 300 km being too small. However, it would have to be increased to 475 km to fully account for the disparity, which is likely too high for the bulk of the irregularities.

The differences in observed irregularity speed between the Cyg A and Cas A lines of sight are more likely to be the result of their different positions on the sky. At both times shown in Fig. 5, Cyg A was in the western part of the sky at azimuths (clockwise from north) of about −60°; Cas A was in the north/northeast with azimuths ∼0°–30°. Both sources were at elevations of ∼60°. Thus, if the irregularities were drifting eastward at ∼7 m s^{-1}, this would have less of an impact on the Cyg A observations, being closer to parallel to its line of sight. To be a bit more specific, the dot products of the horizontal components of the line of sight unit vectors for the two sources are near zero (−0.001 and 0.1 at 03 and 05 UT, respectively). This implies that a plausible scenario is one in which the irregularities were drifting at ∼7 m s^{-1} to the southeast at a bearing of ∼120° (i.e., anti-parallel to the Cyg A line of sight).

2.2 The View from Space

To obtain further insight into the nature of the 12–13 Oct. mid-latitude trough and the irregularities associated with it, data from the Swarm and Ionospheric Connection Explorer (ICON) satellites were analyzed. The Swarm constellation made multiple nighttime passes over the North American region during 11–14 Oct. 2021 timeframe. The left columns of Fig. 6 show the electron density measured by each Swarm satellite's Langmuir probe as a function of latitude during one nighttime pass per day within this period. The median longitude and universal time for each pass is printed above the corresponding panel. These measurements were made in the topside at altitudes of ∼450–500 km.

These plots show a similar pattern as suggested by the TEC and bottom-side data shown in Fig. 1. Specifically, a trough appears just below 50° latitude on the 12$^{\text{th}}$ and moves equatorward on the 13$^{\text{th}}$ where it has a very sharp boundary near 30° latitude,

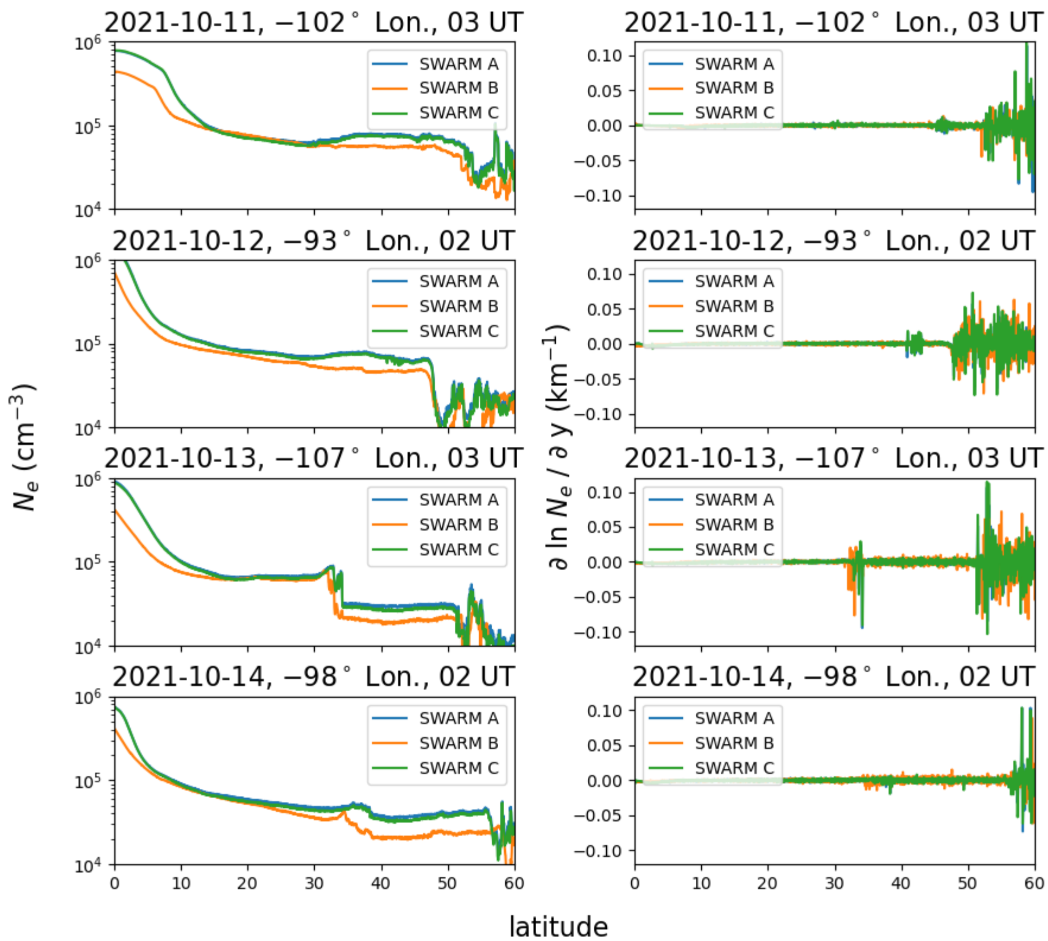

Figure 6. Left column: From 11–14 Oct. 2021, electron densities measured with the SWARM satellites at altitudes of ∼450–500 km during nighttime passes over North America. Right column: The spatial derivative along the path of the satellite of $\ln N_e$ (i.e., the reciprocal of the density gradient scale length) for each pass shown in the corresponding panel on the left.

which all but disappears by the 14$^{\text{th}}$. The spatial derivative of $\ln N_e$ along each satellite's poleward path is shown in the panels on the right, which is the reciprocal of the density scale length in that direction. One can see that this reaches a minimum near the southern boundary of the trough on the 13$^{\text{th}}$ with a value of $\sim$0.05–0.1 km^{-1} in the equatorward direction, or a scale length of $\sim$10–20 km.

To specifically examine structures on smaller scales, a portion of the Swarm N_e was examined close to the steep drop-off near the trough boundary on the 13$^{\text{th}}$. This is shown in the upper panel of Fig. 7, which shows N_e as a function of latitude again for the three Swarm satellites, but zoomed in near the edge of the trough. A Fourier transform was performed for each satellite in the region 32°–34.5° latitude, which is highlighted in color in the upper panel of Fig. 7. The resulting power spectra are plotted in the lower panel and are reasonably well fit by nearly a single power law over $\sim$1.5 decades in spatial frequency/wavelength. The black curve shows the case for a Kolmogorov-like turbulent spectrum with an outer scale of 200 km, which matches the spectra quite well.

As suggested in Sec. 1, the extreme density gradient near the edge of the trough suggests that a mechanism such as the GDI could be driving irregularity formation. For this to be the case, the ion velocity relative to that of the neutral gas must be in the direction of the density gradient, which is predominantly southward in this case. Mathematically, this can be expressed in the form of an approximate one-dimensional GDI growth rate $\gamma_0 = V_L/L$, where V_L is the projection of the ion velocity relative to the neutral velocity in the direction of the N_e gradient and L is the N_e scale length in that direction (Sojka et al., 1998). Thus, the growth rate is large if L is small and/or V_L is large. The Swarm Langmuir probe data imply that on the 13$^{\text{th}}$, $L \simeq 10$–20 km, which is relatively small.

In this case, the quantity V_L can be large due to high southward ion drifts and/or strong northward neutral winds. To explore these possibilities, data from the ICON satellite's Ion Velocity Meter (IVM) and Michelson Interferometer for Global High-resolution Thermospheric Imaging (MIGHTI) were obtained. During the night of the 13$^{\text{th}}$, the closest IVM F-region ion drift measurements to North America were near 25°N, 150°W at an altitude of $\sim$580 km. These showed drifts of $\sim$30 m s^{-1} toward the southwest (bearing of around $-165°$), which is not particularly large but is in the right direction for the GDI. The DLITE data presented in Sec. 2.1 implied drifts over New Mexico of $\sim$7 m s^{-1} and likely toward the southeast, which are also in the right approximate direction but even smaller.

In contrast to the regional ion drifts, the F-region neutral winds measured by MIGHTI were relatively large, $\sim$100-200 m s^{-1}, and northward. This is shown in Fig. 8 where wind vectors from nighttime passes of ICON over the region are plotted for an altitude of 301 km (red arrows) with ROTI maps computed using the entire approximate nighttime interval of 00–12 UT for 11-14 Oct. 2021. One can see that the winds point almost directly perpendicular to the elevated ROTI regions at the trough edge on 12 and 13 Oct. and in the opposite direction of the N_e gradient (i.e., roughly northward). This puts V_L at around 150 m s^{-1}, which, when combined with the Swarm data, implies $\gamma_0 \approx 0.01$ s^{-1} or a time scale of $\sim$100 s.

The N_e power spectrum shown in Fig. 7 is consistent with the spectrum of a turbulent cascade that could be driven by the GDI. With a unique combination of GPS and DLITE data, we can test how well this turbulent approximation explains the irregularities observed by these sensors. As described by Helmboldt et al. (2021), DLITE scintillation measurements are converted to measurements of the C_kL index assuming a Kolmogov spectrum. This is essentially an extrapolation from the 35-MHz Fresnel scale that dominates DLITE-observed scintillations to a scale of 1 km at which C_kL acts as a normalization factor for the full fluctuation spectrum. At a distance of a few hundred km, this Fresnel scale is $\sim$2 km, and so this is not a particularly extreme extrapolation.

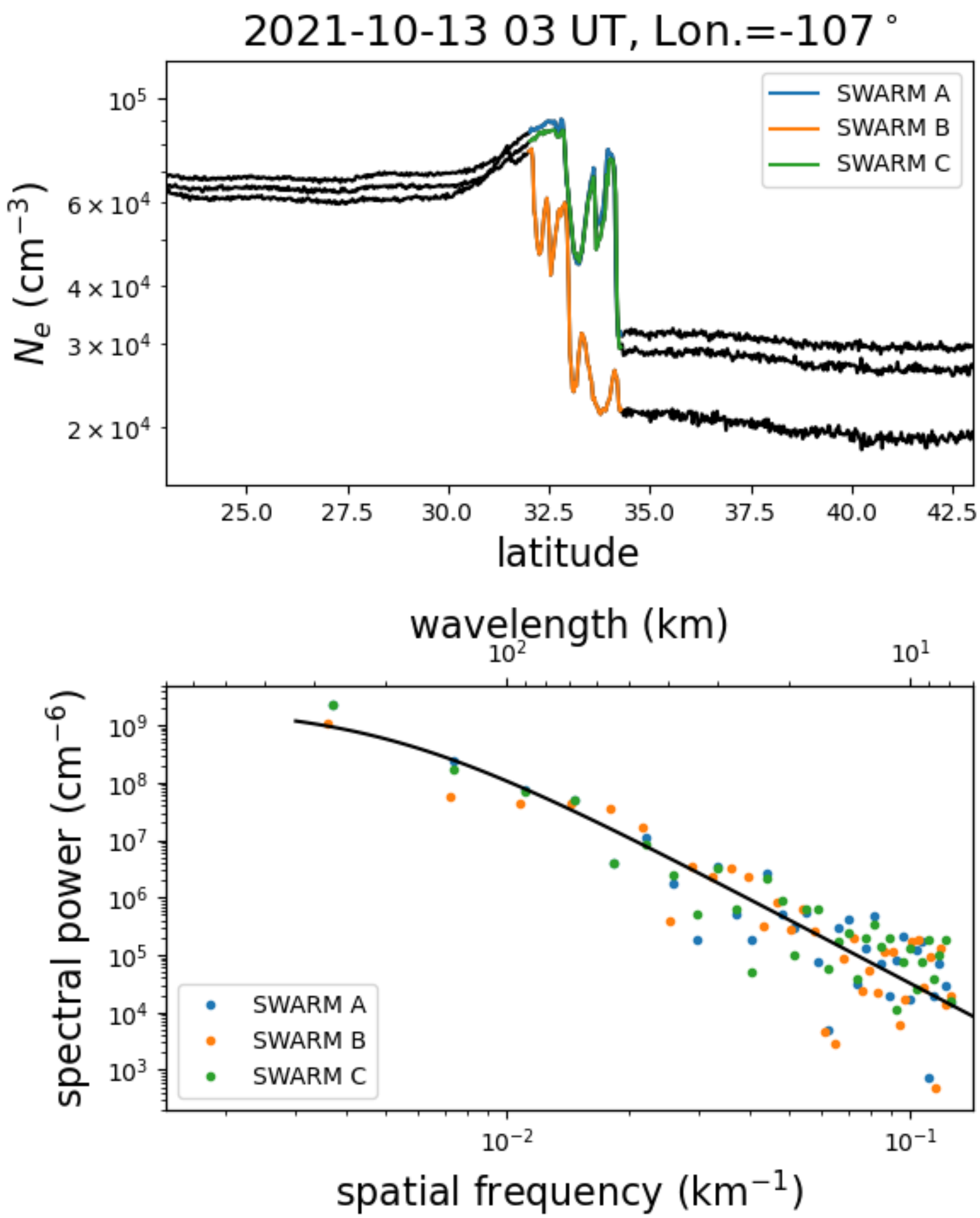

Figure 7. Upper: The electron density time series from the SWARM satellites on 13 Oct. 2021 shown in the left panels of Fig. 6, but with the region of the steep density gradient highlighted. Lower: The fluctuation spectra of the highlighted regions in the upper panel. The black curve is a fit of a power law with a Kolmogorov-like slope and an outer scale of 200 km.

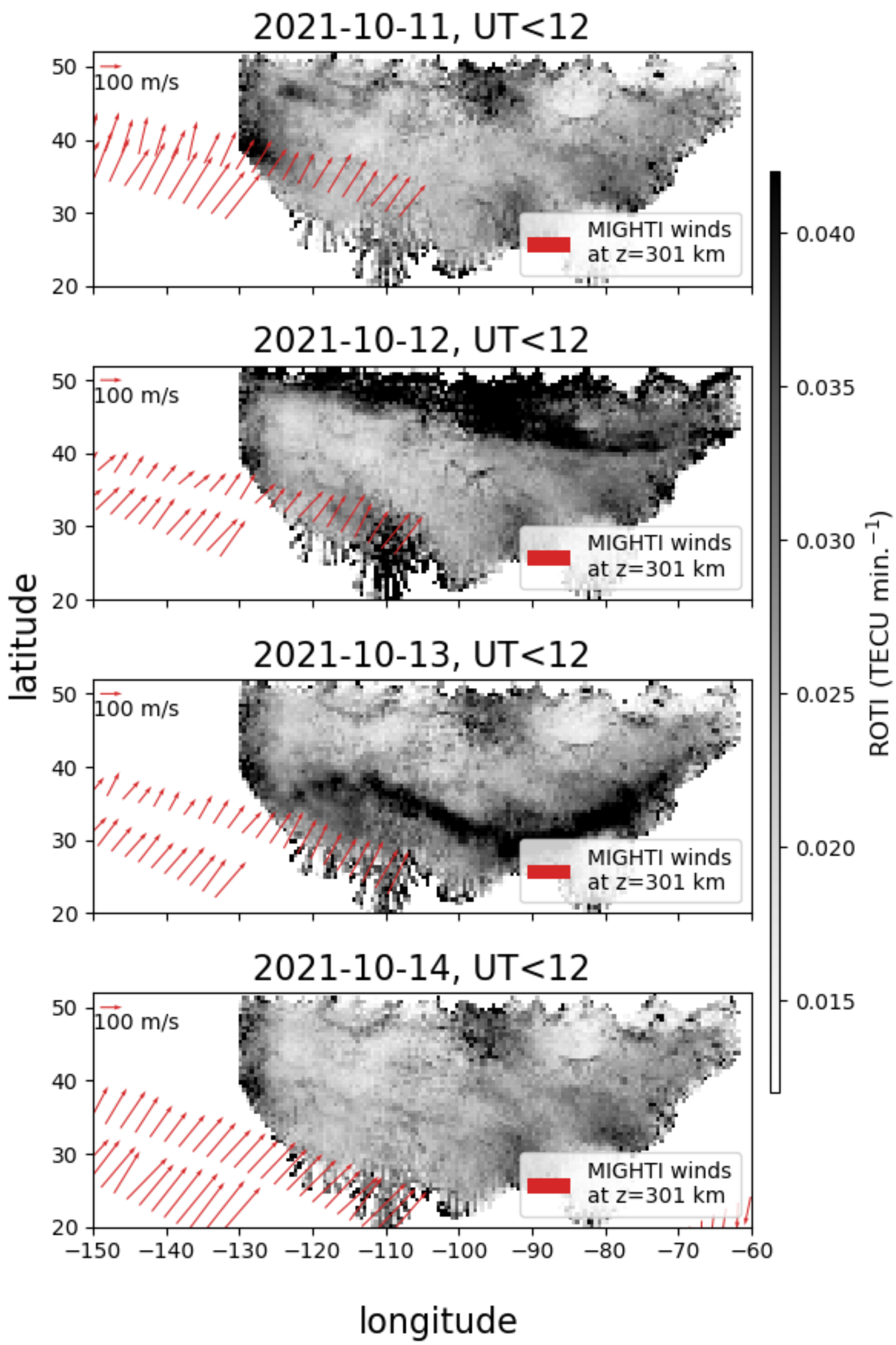

Figure 8. Neutral winds (red vectors) at a height of 301 km from the MIGHTI instrument onboard the ICON satellite from 11–14 Oct. 2021 with maps of ROTI averaged over the full 00–12 UT range.

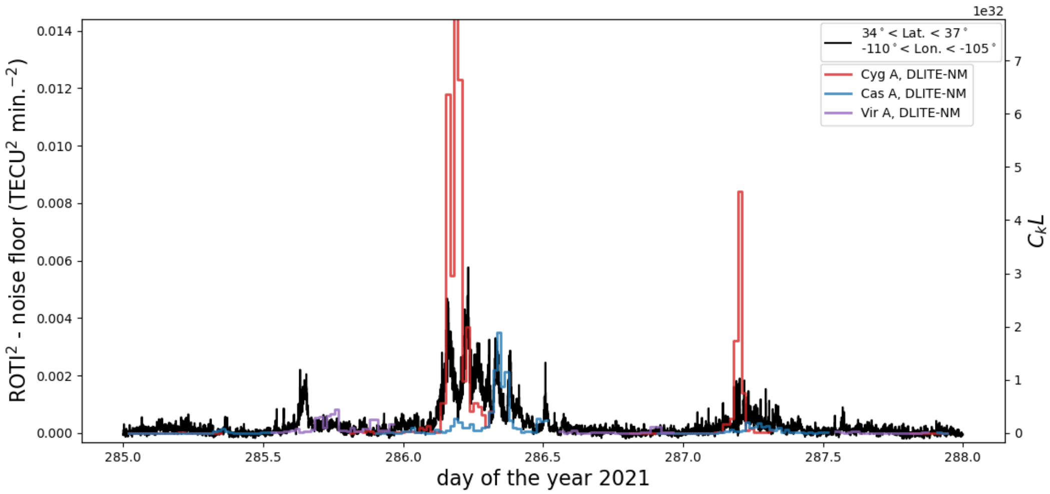

Figure 9. For 12–14 Oct. 2021, a time series of ROTI^2 averaged within the region 34°$<$ Lat.$<$ 37° and $-110°$ $<$ Lon. $<$ $-105°$ at a resolution of one minute (black curve) meant to overlap with the region covered by the DLITE-NM pierce points toward Cyg A and Cas A. A median noise floor value of 4×10^{-4} TECU^2 min.$^{-2}$ has been subtracted. Values for C_kL derived from the DLITE-NM data are plotted in red and blue for Cyg A and Cas A, respectively, which follow the ordinate on the right. The two ordinates match for the median estimated conversion factor between ROTI^2 in units of TECU^2 min.$^{-2}$ and C_kL of 5.4×10^{34}. The maximum C_kL for Cyg A, which is outside the plot window, is 1×10^{34}.

In contrast, ROTI is sensitive to the integrated impact of the entire irregularity spectrum up to the largest scales measurable with the data. As Carrano et al. (2019) showed, ROTI can be converted to C_kL and vice versa but again, a power law spectrum was assumed. An examination of the geometry of the CONUS GPS observations used to make the ROTI maps combined with the conversion given by Carrano et al. (2019) and an assumed Kolmogorov-like spectral index gives a median conversion factor from from ROTI^2 in units of TECU^2 min.$^{-2}$ to C_kL of 5.4×10^{34}. In Fig. 9, a time series of ROTI^2 at one-minute resolution within the region between 34° and 37° latitude and $-110°$ and $-105°$ longitude is plotted. This region was chosen to encompass the area traversed by the pierce points of the lines of sight from DLITE-NM toward Cyg A and Cas A for elevations $>20°$. A median noise floor of 4×10^{-4} TECU^2 min.$^{-2}$ was subtracted to approximately correct for noise biasing.

For comparison, time series of C_kL calculated with DLITE-NM scintillation data for Cyg A (red) and Cas A (blue) are also plotted and follow a separate ordinate to the right. The two ordinates are scaled such that the curves will match for the median conversion factor given above. Values of C_kL for a third source, Virgo A (Vir A), are also plotted (in purple) to provide 24 hours of coverage per day. While Vir A is several times fainter than Cyg A or Cas A, it is still bright enough to typically exhibit scintillations significantly above the system noise (Helmboldt et al., 2021), and it is visible at times when the other two are not. One can see that while there is not a one-to-one correspondence between ROTI^2 and DLITE-derived C_kL, elevated ROTI often coincides with larger C_kL values, especially during the active periods on 13 and 14 Oct.

Additionally, there are significant differences between the values for Cyg A and Cas A, which typically differ by a factor of $\sim$2 (Helmboldt et al., 2021), but are as much as 100 times different in this case (the maximum C_kL for Cyg A was 1×10^{34} and is outside the plot window of Fig. 9). This indicates a relatively patchy distribution of irregularities that likely drives down ROTI^2, which is averaged over a significant area. This patchiness also likely contributes to the temporal variability of ROTI^2, which shows multiple peaks on 13 Oct. that are spaced by ∼1 hour from one another. Based on DLITE and IVM data, the irregularities were drifting at ∼7–30 m s^{-1}, implying that the 1-hour quasi-periodic ROTI structure could be from patches spaced by ∼25–110 km. The sometimes substantial differences between Cyg A and Cas A are consistent with this given that their pierce points were separated by ∼220 km.

3 Conclusions

The combination of ground- and space-based data presented here paint a relatively clear picture of irregularity formation along the edge of a storm-induced mid-latitude trough over North America in Oct. 2021. The trough begins to appear at high latitudes on the 11$^{\text{th}}$ as the Dst index begins to decrease. At the onset of the storm on the 12$^{\text{th}}$ when Dst reaches a minimum, the trough begins to move equatorward and the impact of irregularities at the edge of the trough become apparent within GPS data as increased ROTI. By the 13$^{\text{th}}$, the edge of the trough had become very sharply defined and descended down to ∼30° latitude. There, irregularities within a relatively narrow strip (∼5° wide) along the boundary caused inflated ROTI, strong 35 MHz scintillations observed from New Mexico, and spread-F within the ionograms from multiple digisonde stations. While the electron density and TEC remained relatively depleted on the 14$^{\text{th}}$, the sharp equatorward edge and its associated irregularities were gone by this time.

Spaced-based measurements of F-region N_e and neutral winds revealed that near the trough edge, conditions for the GDI were optimal with an e-folding growth time of about 100 s. The power spectrum of N_e fluctuations near the boundary region was consistent with a turbulent cascade with an outer scale of about 200 km. Comparisons of ROTI measurements near New Mexico with C_kL values derived from 35 MHz scintillations were also roughly consistent with the assumption of a Kolmogorov-like spectrum, albeit with a relatively patchy spatial distribution of irregularities. The detailed structure of scintillation-induced artifacts within 35 MHz images of cosmic radio sources from New Mexico on the 13$^{\text{th}}$ also revealed that the irregularities were moving relatively slowly, ∼7 m s^{-1}, likely in the southeast direction. During this time, the trough edge remained relatively stable for several hours, and it appears the irregularities that formed there did not stray far over that time.

While limited conclusions can be drawn from a single case study, these result can provide motivation for follow-up investigations of the role the GDI plays in irregularity formation near mid-latitude troughs. This hypothesis is highly testable as one would only expect irregularities to form near a well-defined edge if the neutral winds and/or ion drifts were strong and pointed in the optimal direction(s). This is particularly relevant to forecasting of strong mid-latitude irregularities that are much smaller than the typical grid size of global or even regional ionospheric models. If the GDI is a primary driver and if such models can accurately predict trough formation and evolution, then the GDI growth rate can be calculated from simulated data and an irregularity probability may be estimated. For instance, Huba and Liu (2020) used a combination of space-based data and high-resolution simulations to show that the in the equatorial region, the generalized Rayleigh-Taylor instability growth rate was a good indicator of the likelihood of plasma bubble formation. However, achieving something similar with trough-driven irregularities at mid-latitudes would require a foundation of empirical data to quantify the likelihood of irregularity formation for a given GDI growth rate. Hence, such follow-up statistical studies may be of great interest.

Independent of any future follow-on work, this study stands as a unique look into a relatively well-known phenomenon. By combining several different remote sensing and in situ measurements surrounding the 12 Oct. 2021 geomagnetic storm, the mid-latitude trough was shown to be an effective engine for the formation of irregularities that wreak havoc on radio frequency systems from frequencies of a few MHz to 1.5 GHz.

Acknowledgments

Derived DLITE data products used within this publication are available at `https://lda10g.alliance.unm.edu/~dlite`. Development and testing of the DLITE system were supported by the Defense Advanced Research Agency (DARPA) Space Environment Exploitation (SEE) program. GPS RINEX data were obtained from the IGS (`https://cddis.nasa.gov`), CORS (`https://www.ngs.noaa.gov/CORS/data.shtml`), SOPAC (`http://garner.ucsd.edu`), and UNAVCO (`https://www.unavco.org/data/data.html`) databases. Vertical TEC data were obtained from the Madrigal database at `http://millstonehill.haystack.mit.edu`. Digisonde data were obtained from the Global Ionosphere Radio Observatory (`http://giro.uml.edu`). Geomagnetic indices were obtained from the NASA OMNIWeb Plus service (`https://omniweb.gsfc.nasa.gov`). Swarm data were obtained from `https://swarm-diss.eo.esa.int`. ICON data from the IVM and MIGHTI instruments were obtained from FTP servers with links given at `https://icon.ssl.berkeley.edu/Data/Data-Product-Matrix`.

References

Carrano, C. S., Groves, K. M., & Rino, C. L. (2019). On the relationship between the rate of change of total electron content index (roti), irregularity strength (ckl), and the scintillation index (s4). *Journal of Geophysical Research: Space Physics*, *124*(3), 2099-2112. Retrieved from `https://agupubs.onlinelibrary.wiley.com/doi/abs/10.1029/2018JA026353` doi: https://doi.org/10.1029/2018JA026353

Fallows, R. A., Coles, W. A., McKay-Bukowski, D., Vierinen, J., Virtanen, I. I., Postila, M., ... Stuurwold, K. (2014). Broadband meter-wavelength observations of ionospheric scintillation. *Journal of Geophysical Research: Space Physics*, *119*(12), 10,544-10,560. Retrieved from `https://agupubs.onlinelibrary.wiley.com/doi/abs/10.1002/2014JA020406` doi: https://doi.org/10.1002/2014JA020406

Foster, J. C., Erickson, P. J., Coster, A. J., Goldstein, J., & Rich, F. J. (2002). Ionospheric signatures of plasmaspheric tails. *Geophysical Research Letters*, *29*(13), 1-1-1-4. Retrieved from `https://agupubs.onlinelibrary.wiley.com/doi/abs/10.1029/2002GL015067` doi: https://doi.org/10.1029/2002GL015067

Helmboldt, J. F., Markowski, B. B., Bonanno, D. J., Clarke, T. E., Dowell, J., Hicks, B. C., ... Taylor, G. B. (2021). The deployable low-band ionosphere and transient experiment. *Radio Science*, *56*(7), e2021RS007298. Retrieved from `https://agupubs.onlinelibrary.wiley.com/doi/abs/10.1029/2021RS007298` (e2021RS007298 2021RS007298) doi: https://doi.org/10.1029/2021RS007298

Helmboldt, J. F., & Zabotin, N. (2022). An observed trend between midlatitudes km-scale irregularities and medium-scale traveling ionospheric disturbances. *Radio Science*, *57*(5), e2021RS007396. Retrieved from `https://agupubs.onlinelibrary.wiley.com/doi/abs/10.1029/2021RS007396` (e2021RS007396 2021RS007396) doi: https://doi.org/10.1029/2021RS007396

Hicks, B. C., Paravastu-Dalal, N., Stewart, K. P., Erickson, W. C., Ray, P. S., Kassim, N. E., ... Weiler, K. W. (2012, October). A Wide-Band, Active Antenna System for Long Wavelength Radio Astronomy. *Publications of the Astronomical Society of the Pacific*, *124*, 1090-1104. doi: 10.1086/668121

Huba, J. D., & Liu, H.-L. (2020). Global modeling of equatorial spread f with sami3/waccm-x. *Geophysical Research Letters*, *47*(14), e2020GL088258.

Retrieved from https://agupubs.onlinelibrary.wiley.com/doi/abs/10.1029/2020GL088258 (e2020GL088258 10.1029/2020GL088258) doi: https://doi.org/10.1029/2020GL088258

Krankowski, A., Shagimuratov, I. I., Ephishov, I. I., Krypiak-Gregorczyk, A., & Yakimova, G. (2009, June). The occurrence of the mid-latitude ionospheric trough in GPS-TEC measurements. *Advances in Space Research*, *43*(11), 1721-1731. doi: 10.1016/j.asr.2008.05.014

Ledvina, B. M., Makela, J. J., & Kintner, P. M. (2002). First observations of intense gps l1 amplitude scintillations at midlatitude. *Geophysical Research Letters*, *29*(14), 4-1-4-4. Retrieved from https://agupubs.onlinelibrary.wiley.com/doi/abs/10.1029/2002GL014770 doi: https://doi.org/10.1029/2002GL014770

Linson, L. M., & Workman, J. B. (1970). Formation of striations in ionospheric plasma clouds. *Journal of Geophysical Research (1896-1977)*, *75*(16), 3211-3219. Retrieved from https://agupubs.onlinelibrary.wiley.com/doi/abs/10.1029/JA075i016p03211 doi: https://doi.org/10.1029/JA075i016p03211

Rodrigues, F. S., Socola, J. G., Moraes, A. O., Martinis, C., & Hickey, D. A. (2021). On the properties of and ionospheric conditions associated with a mid-latitude scintillation event observed over southern united states. *Space Weather*, *19*(6), e2021SW002744. Retrieved from https://agupubs.onlinelibrary.wiley.com/doi/abs/10.1029/2021SW002744 (e2021SW002744 2021SW002744) doi: https://doi.org/10.1029/2021SW002744

Schunk, R. W., Banks, P. M., & Raitt, W. J. (1976, July). Effects of electric fields and other processes upon the nighttime high-latitude F layer. *Journal of Geophysical Research*, *81*(19), 3271. doi: 10.1029/JA081i019p03271

Shinbori, A., Otsuka, Y., Tsugawa, T., Nishioka, M., Kumamoto, A., Tsuchiya, F., ... Nishitani, N. (2018). Temporal and spatial variations of storm time midlatitude ionospheric trough based on global gnss-tec and arase satellite observations. *Geophysical Research Letters*, *45*(15), 7362-7370. Retrieved from https://agupubs.onlinelibrary.wiley.com/doi/abs/10.1029/2018GL078723 doi: https://doi.org/10.1029/2018GL078723

Sojka, J. J., Subramanium, M. V., Zhu, L., & Schunk, R. W. (1998, November). Gradient drift instability growth rates from global-scale modeling of the polar ionosphere. *Radio Science*, *33*(6), 1915-1928. doi: 10.1029/98RS02490